

An uncontaminated measurement of the escaping Lyman continuum at $z \sim 3$

Anthony J. Pahl ¹★, Alice Shapley,¹ Charles C. Steidel,² Yuguang Chen ² and Naveen A. Reddy³

¹Department of Physics and Astronomy, University of California, Los Angeles, CA 90095, USA

²Cahill Center for Astronomy and Astrophysics, California Institute of Technology, MC249-17, Pasadena, CA 91125, USA

³Department of Physics and Astronomy, University of California Riverside, Riverside, CA 92521, USA

Accepted 2021 May 6. Received 2021 May 5; in original form 2021 April 5

ABSTRACT

Observations of reionization-era analogues at $z \sim 3$ are a powerful tool for constraining reionization. Rest-ultraviolet observations are particularly useful, in which both direct and indirect tracers of ionizing-photon production and escape can be observed. We analyse a sample of 124 $z \sim 3$ galaxies from the Keck Lyman Continuum Spectroscopic Survey, with sensitive spectroscopic measurements of the Lyman continuum region. We present a method of removing foreground contamination from our sample using high-resolution, multiband *Hubble Space Telescope* imaging. We re-measure the global properties of the cleaned sample of 13 individually detected Lyman continuum sources and 107 individually undetected sources, including a sample-averaged absolute escape fraction of $f_{\text{esc, abs}} = 0.06 \pm 0.01$ and a sample-averaged ratio of ionizing to non-ionizing ultraviolet flux density of $\langle f_{900}/f_{1500} \rangle_{\text{out}} = 0.040 \pm 0.006$, corrected for attenuation from the intergalactic and circumgalactic media. Based on composite spectra, we also recover a strong positive correlation between $\langle f_{900}/f_{1500} \rangle_{\text{out}}$ and Ly α equivalent width ($W_{\lambda}(\text{Ly}\alpha)$) and a negative correlation between $\langle f_{900}/f_{1500} \rangle_{\text{out}}$ and UV luminosity. As in previous work, we interpret the relationship between $\langle f_{900}/f_{1500} \rangle_{\text{out}}$ and $W_{\lambda}(\text{Ly}\alpha)$ in terms of the modulation of the escape of ionizing radiation from star-forming galaxies based on the covering fraction of neutral gas. We also use a $W_{\lambda}(\text{Ly}\alpha)$ -weighted $\langle f_{900}/f_{1500} \rangle_{\text{out}}$ to estimate an ionizing emissivity from star-forming galaxies at $z \sim 3$ as $\epsilon_{\text{LyC}} \simeq 5.5 \times 10^{24} \text{ erg s}^{-1} \text{ Hz}^{-1} \text{ Mpc}^{-3}$. This estimate, evaluated using the uncontaminated sample of this work, affirms that the contribution of galaxies to the ionizing background at $z \sim 3$ is comparable to that of active galactic nuclei.

Key words: galaxies: high-redshift – dark ages, reionization, first stars – cosmology: observations.

1 INTRODUCTION

Reionization, the last major phase transition of the Universe, describes the ionization of the Hydrogen gas in the inter-galactic medium (IGM) in the first billion years of the Universe’s history. Since the reionization process ends by $z \sim 6$ (Fan, Carilli & Keating 2006; Robertson et al. 2015; Planck Collaboration 2016) and the number density of luminous quasi-stellar objects (QSOs) drops off sharply beyond $z \sim 2$ (Shen et al. 2020), the prevailing notion is that ionizing radiation leaking from early star-forming galaxies drives the process of reionization (e.g. Bouwens et al. 2015; Parsa, Dunlop & McLure 2018).

A number of observational constraints and challenges prevent a straightforward analysis of the galaxies that contribute strongly to the ionizing background during reionization. While we can chart the abundance of star formation rates (SFRs) as a function of redshift (Madau & Dickinson 2014), the difficulty lies in converting the cosmic SFR density (ρ_{SFR}) into an ionizing emissivity, a key factor in dictating the evolution of the IGM neutral fraction (Bouwens et al. 2015; Robertson et al. 2015). One of the essential parameters for converting between ρ_{SFR} and the ionizing emissivity is $f_{\text{esc, abs}}$, the absolute escape fraction of ionizing radiation produced in H II

regions that evades absorption by neutral-phase gas and dust in the ISM. Unfortunately, it is not possible to constrain $f_{\text{esc, abs}}$ directly based on measurements during the epoch of reionization considering the drastic drop-off of transmission of ionizing rest-UV continuum through the IGM past $z > 3.5$ (Vanzella et al. 2012; Steidel et al. 2018). Instead, there has been a focus on sources analogous to the $z > 6$ reionizing population but observed at redshifts where the IGM is still transparent to Lyman Continuum (LyC) radiation at $\lambda \leq 912 \text{ \AA}$.

Many of the direct $f_{\text{esc, abs}}$ measurements in the local Universe come from compact galaxies with large [O III]/[O II] ratios and high [O III] $\lambda 5007$ equivalent widths, referred to as ‘Green Peas’ (*HST*/COS; Borthakur et al. 2014; Izotov et al. 2016, 2018, 2021). At higher redshifts ($z \sim 3$), the properties of galaxies and their circumgalactic environments begin to align more with those in the reionization era. Meanwhile, the IGM opacity is still at a level that allows for the direct detection of LyC emission from star-forming galaxies. These aspects make this redshift range compelling for LyC surveys, but the sightline-to-sightline variability in IGM opacity makes the interpretations of individual LyC detections difficult. Thanks to advances in deep optical spectroscopy and narrowband imaging, there have been a handful of individual LyC detections at $z \sim 3$ (e.g. Mostardi et al. 2015; De Barros et al. 2016; Shapley et al. 2016; Vanzella et al. 2016, 2018; Bian et al. 2017). In order to understand the LyC of the full population of galaxies at $z \sim 3$, however, larger and representative ensembles of galaxies with

* E-mail: pahl@astro.ucla.edu

sensitive LyC measurements are required that can smooth out the deviations in the transmission of the IGM through sample averaging.

To this end, the Keck Lyman Continuum Spectroscopic (KLCS) survey (Steidel et al. 2018, hereafter S18) utilized the LRIS double spectrograph on the *Keck I* telescope (Oke et al. 1995; Steidel et al. 2004) to observe 124 $2.75 \leq z \leq 3.4$ galaxies in the rest-UV with the goal of constructing spectral composites that represent global properties of $z \sim 3$ galaxies. S18 reported a sample-averaged absolute escape fraction of $f_{\text{esc, abs}} = 0.09 \pm 0.01$ for their sample after performing spectroscopic contamination rejection as well as fitting Binary Model and Stellar Synthesis (BPASS; Eldridge et al. 2017) templates and physically motivated ISM models to rest-frame UV composite spectra. This sample-averaged $f_{\text{esc, abs}}$ has a robust correction for IGM and circumgalactic medium (CGM) absorption due to the large sample number that went into the calculation. These results are complemented by other large-scale LyC surveys at $z \sim 3$ –4, such as the LACES survey of 61 $z \sim 3.1$ Ly α -emitting galaxies using WFC3/UVIS F336W imaging on *HST* (Fletcher et al. 2019) and the survey of 201 star-forming $z \sim 4$ galaxies drawn from the VUDS survey using VLT/VIMOS spectroscopy (Marchi et al. 2018).

One remaining limitation in interpreting the results of high-redshift LyC surveys is the risk of non-ionizing UV light from foreground objects masquerading as an apparent ionizing signal. From the ground, a $z \sim 3$ galaxy may appear as a coherent object with strong LyC flux density, but higher-resolution imaging can reveal a lower-redshift source nearby along the line of sight that contributes to the observed-frame ~ 3600 Å spectrum. Vanzella et al. (2012) demonstrated the potential pitfalls of line-of-sight contamination in seeing-limited ground-based LyC observations. Building on these ideas, Mostardi et al. (2015, hereafter M15) examined 16 apparent $z \sim 2.85$ LyC leakers identified through ground-based narrowband imaging. Multiband *Hubble Space Telescope* (*HST*) imaging was used to examine the photometric-redshifts of individual subcomponents within the seeing-limited extent of each target. M15 found that 15 out of 16 of the apparent LyC detections were contaminated with foreground signal. The demonstrated efficacy of this methodology and the propensity for line-of-sight contamination highlights the importance of high-resolution, space-based follow-up of LyC detection candidates at $z \sim 3$.

In the current work, we attempt to increase the confidence of the results of one of the largest $z \sim 3$ LyC surveys, the KLCS survey, by examining the strongest LyC sources with *HST* imaging. We specifically targeted the 15 KLCS galaxies with significant (3σ) individual detections of LyC flux in deep Keck/LRIS spectroscopy, as they significantly affect the global statistics of the sample. We simultaneously examined 24 additional galaxies in the sample that fall on the *HST* mosaics but lack individual LyC detections. In addition to searching for foreground contamination in the KLCS sample, this work also serves as an update to S18 by revisiting the key results of the paper using a cleaned sample. Accordingly, our analysis yields a statistically robust, uncontaminated description of the LyC properties of $z \sim 3$ star-forming galaxies.

In Section 2, we describe the KLCS parent sample, the ground-based observation methodology, and the details of the *HST* observations. In Section 3, we present the reduction procedures, photometric analysis including the segmentation of objects with complex morphologies, and subsequent photometric measurements. In Section 4, we detail the search for foreground contamination and present the results of the contamination analysis. Finally, in Section 5, we report updated measurements of the LyC properties of the KLCS sample after contamination removal. We summarize our results in Section 6.

Throughout this paper, we adopt a standard Λ cold dark matter cosmology with $\Omega_m = 0.3$, $\Omega_\Lambda = 0.7$, and $H_0 = 70 \text{ km s}^{-1} \text{ Mpc}^{-1}$. We also employ the AB magnitude system.

2 SAMPLE AND METHODOLOGY

The KLCS survey (S18) utilized the Keck/LRIS spectrograph (Oke et al. 1995; Steidel et al. 2004) to obtain deep rest-UV spectra of an initial target sample of 137 galaxies selected as Lyman Break Galaxies (LBGs) at $2.75 \leq z \leq 3.4$ (for a description of U_nGR selection methodology; see Steidel et al. 2003; Adelberger et al. 2004; Reddy et al. 2012). The LRIS spectra of KLCS galaxies cover the Lyman continuum region (LyC, 880–910 Å), the Ly α feature, and far-UV (FUV) interstellar metal absorption features redward of Ly α . The LRIS observations were taken between 2006 and 2008 across nine different survey fields with integration times per mask of ~ 10 h. Of the 137 galaxies observed, eight objects were removed due to instrumental defects or clear evidence for blending with nearby sources. The remaining 2D and 1D spectra were examined for evidence of spectral blending, where an additional redshift along the line of sight could indicate contamination in the apparent LyC flux of a higher-redshift source. Five galaxies were removed due to apparent spectral blending, resulting in a final sample of 124 galaxies for analysis. S18 examined the ratio of ionizing to non-ionizing UV flux density within the KLCS sample, defined as the average flux density within $880 \leq \lambda_0/\text{Å} \leq 910$ (f_{900}) divided by the average flux density within $1475 \leq \lambda_0/\text{Å} \leq 1525$ (f_{1500}), or $\langle f_{900}/f_{1500} \rangle_{\text{obs}}$. 15 galaxies were significantly detected ($f_{900} > 3\sigma_{900}$, where σ_{900} is the f_{900} measurement uncertainty) and were defined as the LyC detection sample. The remaining 109 galaxies with $f_{900} < 3\sigma_{900}$ were defined as the LyC non-detection sample.

Despite significant efforts to remove foreground contamination from the KLCS sample through examination of the 1D and 2D spectra, high-resolution imaging has previously been required to vet individual detections of leaking LyC (Vanzella et al. 2012, M15). In $z \sim 3$ LyC detections, apparent LyC leakage at ~ 3600 Å may actually originate from a low-redshift component that lies in projection within the angular extent of a clumpy galaxy morphology (e.g. Siana et al. 2015; Vanzella et al. 2016). Thus, we require high-resolution, space-based imaging for spatially resolved photometric-redshift analysis of KLCS LyC detections. These observations enable the consideration of individual subcomponents as potential contaminants. We require imaging in multiple filters to judge the redshift of individual, extracted components. The *HST* $V_{606}J_{125}H_{160}$ filter set is ideal for this type of analysis (M15). At $z = 3.07$, the median redshift of the KLCS detection sample, the J_{125} and H_{160} band filters are situated on either side of the Balmer break. These filters are shown in Fig. 1 along with the spectral energy distribution (SED) typical of $z \sim 3$ LBGs from the BPASS set of stellar-population models (Stanway & Eldridge 2018) redshifted to $z = 3.07$. Also displayed is the same BPASS SED at $z = 1.50$, representing a low-redshift interloper. At $z \sim 3$, the $J_{125} - H_{160}$ colour is expected to reflect the Balmer break, while at lower redshift, $J_{125} - H_{160}$ colour is expected to be flatter as both bands probe redward of the break. Additionally, at $z \sim 3$, $V_{606} - J_{125}$ is sensitive to the rest-frame UV spectral slope that provides information on the stellar age and reddening of the galaxy. At lower redshift, the Balmer break passes between the V_{606} and J_{125} bands.

We observed 14 KLCS LyC detection candidates with ACS/F606W (V_{606}), WFC3/F125W (J_{125}), and WFC3/F160W (H_{160}) on *HST* as a part of Cycle 25 Program ID 15287 (PI: Shapley). The observations took place between 2017 and 2019 in five separate LBG survey fields (Q0933, Q1422, DSF2237b, Q1549, and

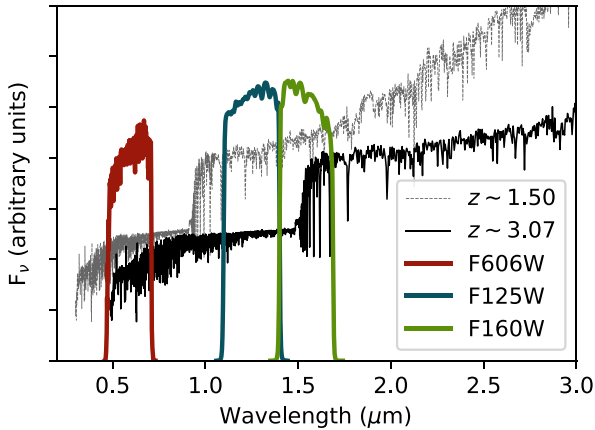


Figure 1. *HST* $V_{606}J_{125}H_{160}$ filter set in wavelength space in relation to a characteristic SED from BPASS (Stanway & Eldridge 2018) shown at different redshifts. This SED was generated with 100 Myr constant star-formation history and solar metallicity, and was reddened using $E(B - V) = 0.2$ and assuming a Calzetti et al. (2000) extinction curve. The black curve indicates the SED shifted to $z = 3.07$, the median redshift of the LyC detection sample. At this redshift, the $J_{125} - H_{160}$ colour probes the 4000 Å Balmer break. The grey curve shows the SED shifted to $z = 1.5$, a redshift typical of low-redshift interlopers. At lower redshift, the $V_{606} - J_{125}$ probes the Balmer break.

Westphal) across seven ACS pointings and 11 WFC3 pointings. The observations within each field were designed to cover the 14 LyC detection candidates with apparent LyC detections but no multiband *HST* data, whereas Q1549-C25 had already been analysed by Shapley et al. (2016). We found the most efficient combination of pointings in each field that covered all apparent LyC detections with V_{606} , J_{125} , and H_{160} . Coincidentally, we covered with all three filters an additional 24 KLCS sources lacking individual LyC detections. These pointings are shown in Fig. 2 alongside KLCS sources covered by all three filters. An additional 11 KLCS LyC non-detections were covered by at least one filter. Each pointing was observed for three orbits per filter, or ~ 7000 s of exposure time. The total duration of the program was 87 orbits, required to ensure $>10\sigma$ detections in V_{606} for potential contaminant components, based on the faintest f_{900} (i.e. observed 3600 Å flux density) values of the detection sample and assuming (at worst) a flat SED between ~ 3600 Å and V_{606} . We executed each orbit using four-point DITHER-BOX dither patterns for ACS/WFC pointings and four-point DITHER-LINE patterns for WFC3/IR pointings. For one LyC detection, Q1549-D3, we included previously acquired *HST* $V_{606}J_{125}H_{160}$ imaging from Cycle 20 Program ID 12959 (PI Shapley; M15). We included five orbits of V_{606} in a single pointing and three orbits of J_{125} and H_{160} each in a single pointing to cover this detection. We re-reduced these exposures with the same techniques applied to the more recent Cycle 25 data to provide consistency across the data sets.

3 REDUCTION

In this section, we detail the steps necessary to convert raw *HST* imaging to aligned images and photometric measurements of our targets. Many of the procedures in this section follow those detailed in M15.

3.1 Mosaic generation and point-spread function matching

First, the calibrated, flux-fielded, and charge-transfer-efficiency-corrected (for ACS) exposures were combined and aligned to produce

a single mosaic for each filter and field observed. This reduction step was completed using the DRIZZLEPAC software package (Fruchter et al. 2010). Contained in the package is the task *AstroDrizzle*, that performs automatic cosmic ray rejection and sky subtraction during image combination, as well as the alignment task *TweakReg*. We used *TweakReg* to calculate residual shifts in RA and Dec. by inputting coordinate lists of extended sources that were first measured using SEXTRACTOR (Bertin & Arnouts 1996). After calculating the shifts by comparing the coordinate lists, *TweakReg* performs corrections by re-registering the WCS of each exposure. The individual exposures within each pointing and filter did not require significant re-alignment to one another, save for the F160W imaging of the northern WFC3/IR pointing in the DSF2237b field, in which *HST* experienced a reaction-wheel failure partway through the exposures and required a ~ 0.05 arcsec adjustment.

After averaged mosaics were generated for each pointing and filter combination, the mosaics within each of the five target fields were aligned to one another and registered on the same WCS. The alignment RMS in both RA and Dec. between ACS images of different pointings was ~ 0.005 arcsec and the alignment RMS between WFC3/IR and ACS pointings was ~ 0.01 arcsec. The final V_{606} , J_{125} , and H_{160} mosaics produced by *AstroDrizzle* were generated with matching pixel grids across filters at a pixel scale of 0.03 arcsec px^{-1} and a drop-to-pixel ratio (`final_pixfrac`) of 0.7 to maximize pixel resolution of the morphological features in the V_{606} imaging. These final mosaics were registered to the WCS of the ground-based UGR images (described in Reddy et al. 2012) available for these fields using the task *ccmap* in IRAF and manually generated starlists of ~ 50 unsaturated stars. The typical RMS in alignment between the *HST* mosaics and the ground-based *G* imaging in both RA and Dec. was ~ 0.06 arcsec. The LyC detection candidates in both ground-based imaging and aligned *HST* imaging are shown in the Fig. 3.

For one object, Westphal-CC38, a small area of decreased sensitivity, or ‘blob’ (Sunnquist 2018), was in the vicinity of the object in the WFC3/IR images. To accurately measure the photometry of this object, we used the sky flats of Mack, Olszewski & Pirzkal (2021) that included corrections to the blobs present on the IR detector.

Next, the V_{606} and J_{125} mosaics were smoothed to the same angular resolution as the corresponding H_{160} mosaic to allow for accurate measurement of colours. Hereafter, we refer to the smoothed V_{606} and J_{125} mosaics as $sm(V_{606})$ and $sm(J_{125})$. The point-spread functions (PSFs) for each field and filter were generated using a set of 10–15 bright unsaturated point sources identified manually within each mosaic. We combined these stellar profiles into PSFs using the ASTROPY routine *Photutils* (Bradley et al. 2020). The average Gaussian full width at half-maximum (FWHM) of the V_{606} , J_{125} , and H_{160} PSFs across all fields were 0.100 arcsec, 0.177 arcsec, and 0.183 arcsec, respectively. We used the IRAF routine *psfmatch* to generate and apply kernels matching the V_{606} and J_{125} mosaics to the resolution of the H_{160} PSF. Curve of growth analysis of the $sm(V_{606})$ and $sm(J_{125})$ PSFs with the original H_{160} PSF demonstrated that the fraction of enclosed flux for all three agrees to within 1 percent at 0.5 arcsec. We display the PSF-matched $sm(V_{606})$ and $sm(J_{125})$ and original-resolution H_{160} postage stamps of the LyC detection candidates as well as $V_{606}J_{125}H_{160}$ (for blue, green, and red) false-colour images in Fig. 3. Postage stamps of the non-detections can be found in the Appendix.

3.2 Photometry

In order to make comparable photometric measurements of each detection in multiple filters, we first must define regions correspond-

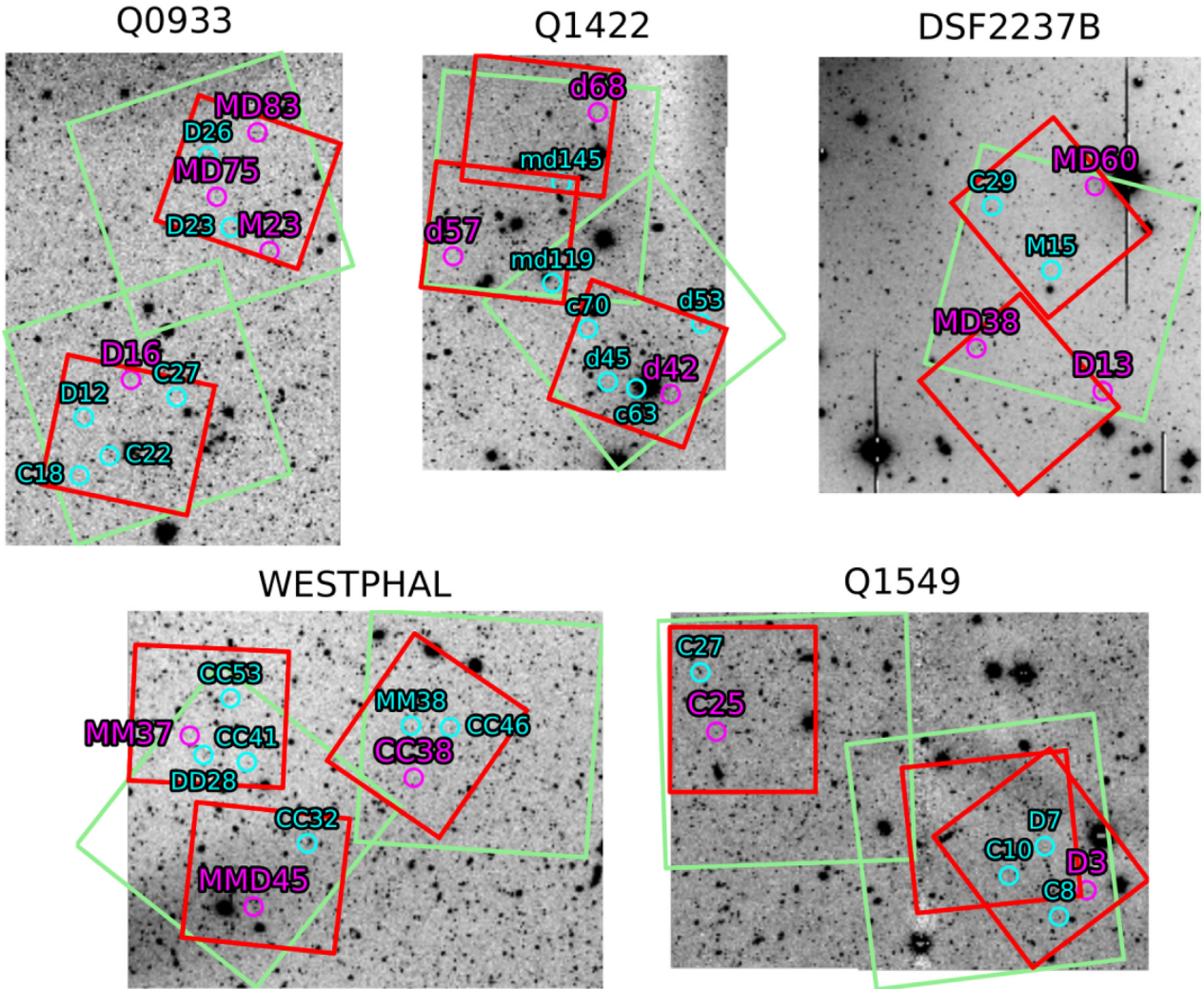


Figure 2. The five fields targeted by our *HST* observing program. In green are the 202 arcsec \times 202 arcsec footprints of the ACS pointings, with imaging taken in the V_{606} band. In red are the 136 arcsec \times 123 arcsec footprints of the WFC3-IR pointings, with imaging taken in J_{125} and H_{160} bands. The magenta circles represent the positions of the 14 LyC detection candidates, while the cyan circles represent the non-detections that lie in the same fields. One LyC detection candidate (Q1549-C25) was not the target of this observing program; the *HST* $V_{606}J_{125}H_{160}$ images are described in M15 (also see Shapley et al. 2016).

ing to the distinct morphological features within each object. To this end, we used *SEXTRACTOR* on the PSF-matched V_{606} image to produce segmentation maps for each object, separating the light profile into different components. We set the detection threshold at four times the background RMS, but reduced this parameter down to three times the background RMS to achieve extraction of subcomponents in individual cases. For background subtraction, we used the ‘local’ method that uses a rectangular annulus around the source to estimate the sky level. We also set the minimum contrast parameter for deblending (*DEBLEND_MINCONT*) to 0 to maximize the number of identified segments.

We placed further requirements on what could be considered a separate component for our analysis. In order to remove spurious detections, we required a minimum area of 30 pixels, corresponding to fully sampling the PSF FWHM at the resolution of H_{160} . We also required each component to be brighter than or equal to 28.5 mag in V_{606} to eliminate all noisy and low ($<10\sigma$) S/N detections. The segmentation maps generated for the LyC detection candidates are shown in the the last column of Fig. 3. For the detection sample, eight were characterized by single-component morphology, five

were separated into two subcomponents, while the final two were characterized by three subcomponents. In the non-detection sample, 13 have a single component, 8 have double components, and 3 have three or more components.

For each subcomponent, we measured $V_{606}J_{125}H_{160}$ photometry from the PSF-matched mosaics. The AB photometric zeropoints of each field and filter combination were calculated using the inverse sensitivity and pivot wavelengths listed in the header of the exposures and were dust corrected using the Galactic reddening maps from Schlegel, Finkbeiner & Davis (1998). The V_{606} photometry was measured isophotally by summing the V_{606} flux of the smoothed image within each region in the *sm*(V_{606}) segmentation map. We used the V_{606} segmentation map to measure the $J_{125}H_{160}$ photometry with *SEXTRACTOR* in dual-image mode.

We determined robust estimates of photometric error empirically. Analytical estimates of error, such as summing the error image calculated from an *AstroDrizzle* exposure-time weight map, do not take into account the covariance between adjacent pixels in averaged mosaics. To reflect this covariance, M15 adopted the empirical approach of Förster Schreiber et al. (2006). The authors created blank

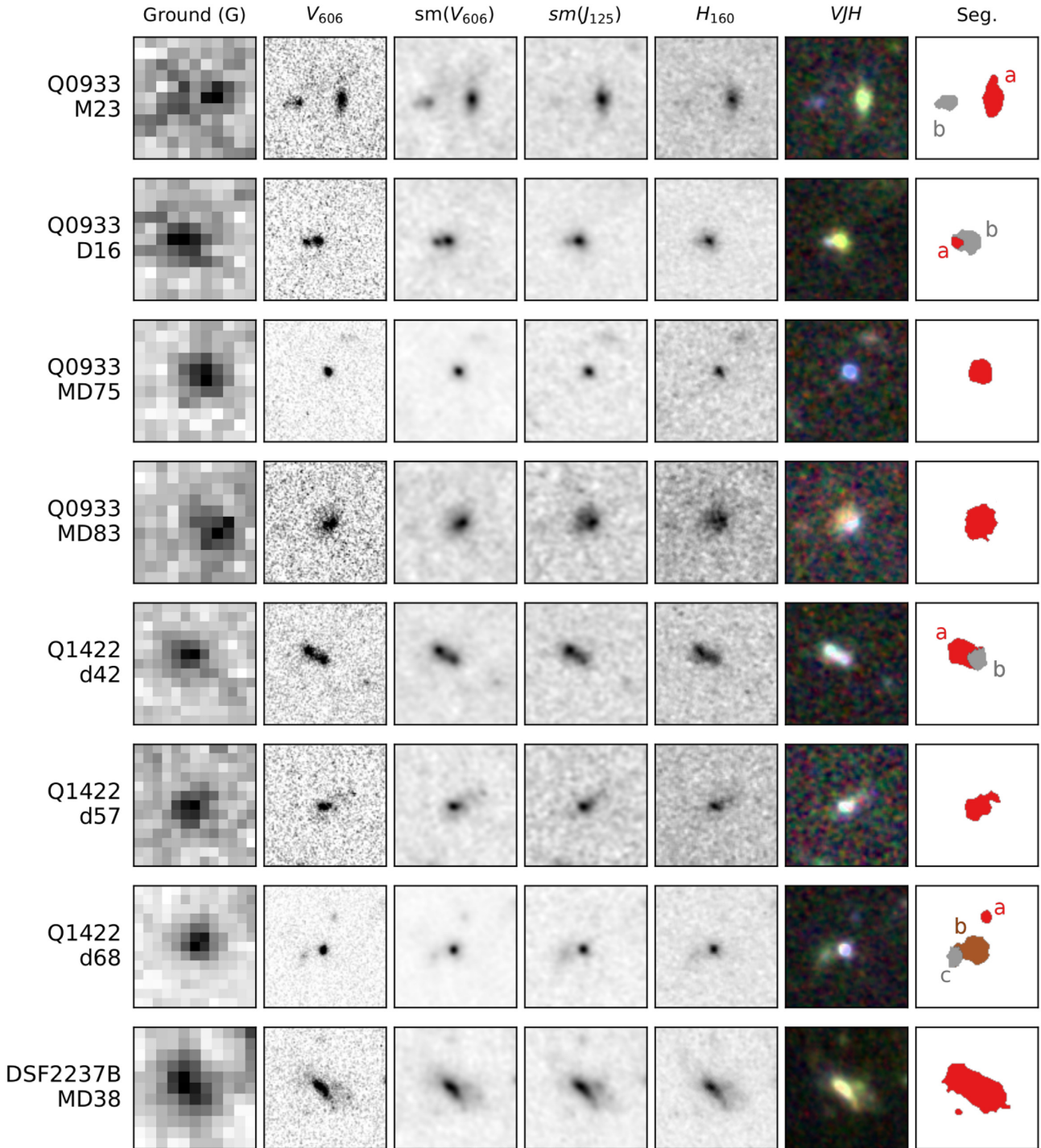
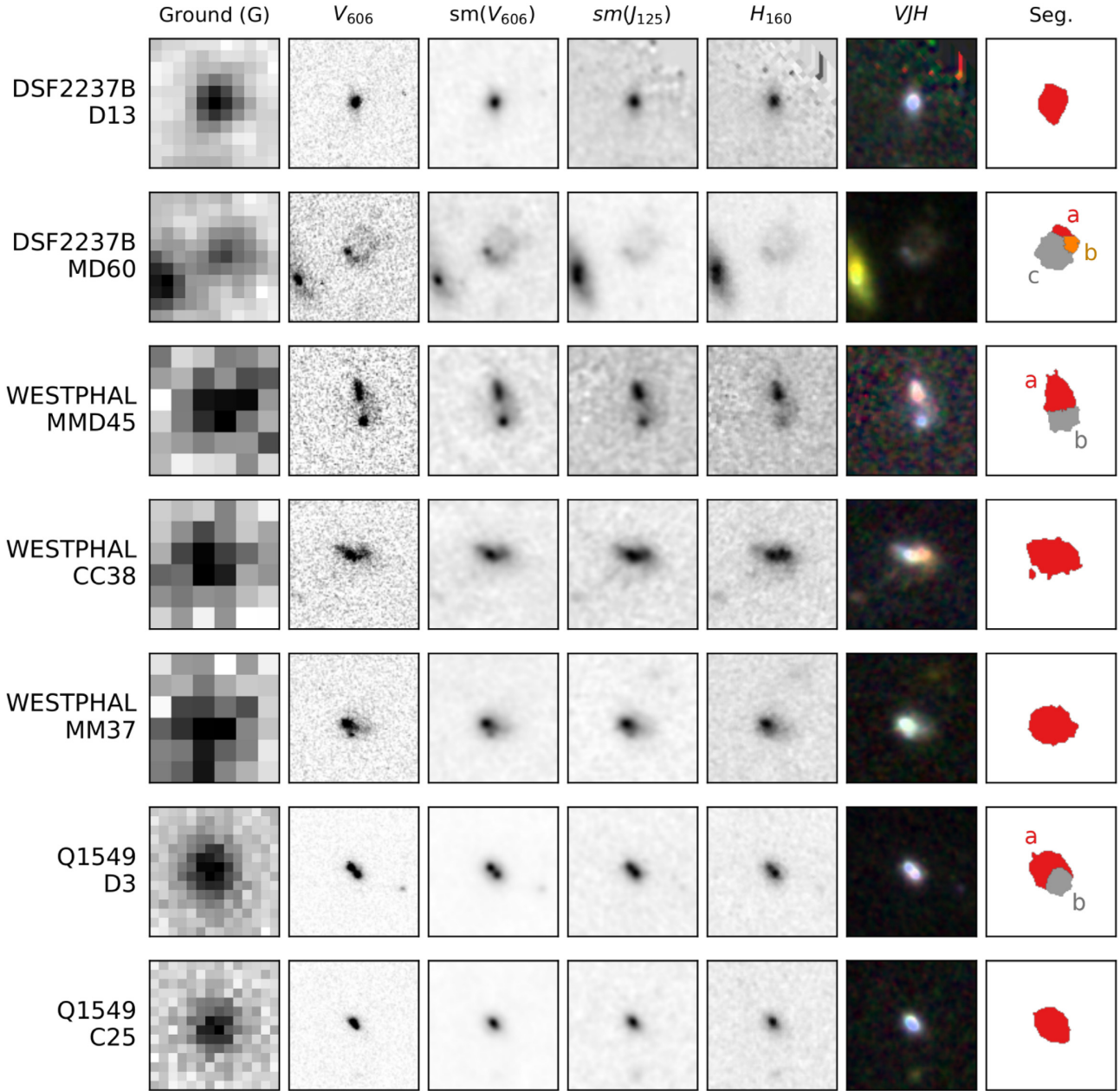


Figure 3. 3 arcsec \times 3 arcsec postage stamps of the 15 LyC detection candidates targeted by *HST*. **First column:** Ground-based G (Reddy et al. 2012). **Second column:** V_{606} at the original resolution. **Third and fourth columns:** V_{125} and J_{125} smoothed to the lower resolution of H_{160} . **Fifth column:** Original-resolution H_{160} . **Sixth column:** False-colour postage stamps. The $sm(V_{606})$, $sm(J_{125})$, and H_{160} images are represented by blue, green, and red, respectively. **Seventh column:** Segmentation map generated by SEXTRACTOR. Separate components extracted by the program are represented by different-coloured regions.

apertures across the mosaics and measured the average signal RMS as a function of radius as a direct estimate of photometric errors. This method accurately captures correlated noise in our mosaics, but does not take into account the spatial deviations in the error image due to differences in exposure times and sky levels. We build upon the M15 method using the covariance correction of Law et al. (2016). We generated 1000 blank circular apertures in each mosaic

in the range of sizes of our components with radii ranging from 0.2 arcsec up to 1.0 arcsec. Within each aperture, we measured the ratio between the standard deviation of the signal within the blank aperture and the sum of the smoothed error image. This ratio is calculated as a function of angular size and indicates the correction of the theoretical error value from *AstroDrizzle* to an empirical one, taking into account correlated noise in the oversampled and smoothed

Figure 3 – *Continued*

mosaics. For a given subcomponent, we take the ratio computed at the subcomponent’s angular size and multiply it by the summed-in-quadrature error image within the $sm(V_{606})$ segmentation map as the 1σ error on the photometric measurement. These photometric measurements for each component in the detection sample can be found in Table 1 as well as the systemic redshift (z_{sys}) from S18. Descriptions of the individually undetected sample can be found in the Appendix. The average 3σ limiting magnitudes across our pointings for the $V_{606}J_{125}H_{160}$ mosaics calculated at $1.5\times$ the average FWHM of the PSF were 30.18, 29.12, and 28.72 mag, respectively.

4 CONTAMINATION REJECTION

As demonstrated by M15, analysis of LyC detection candidates based on high-resolution multiband *HST* imaging is an effective method for identifying low-redshift interlopers. In M15, photometric

redshifts were estimated from the $U_{336}V_{606}J_{125}H_{160}$ magnitudes of each spatially resolved component in the vicinity of a $z \sim 3$ LBG. The identification of foreground interlopers based on these component photometric redshifts led to the removal of 15 apparent LyC leakers at $z \sim 3$ from a sample of 16. These LBGs were all photometric LyC detections that had not yet been cleaned using deep spectroscopy, as described in Section 2 for the KLCS sample. For the current analysis, our photometric measurements are limited to $V_{606}J_{125}H_{160}$, thus preventing us from making well-constrained photometric-redshift fits for each component. However, we are motivated to use $V_{606}J_{125}H_{160}$ photometry to predict contamination by the clear separation of low-redshift contaminants and confirmed high-redshift components of the M15 sample in $V_{606}J_{125}H_{160}$ (i.e. $V_{606} - J_{125}$ versus $J_{125} - H_{160}$) colour–colour space (Fig. 4, upper left), and the positioning of the $V_{606}J_{125}H_{160}$ filters relative to the Balmer break at $z \sim 3$ (Section 2).

Table 1. Photometric measurements of the LyC detection subcomponents.

ID ^a	R.A.	Dec.	$z_{\text{sys}}^{b,c}$	V_{606}	J_{125}	H_{160}
DSF2237B-D13	22:39:27.42	+ 11:49:47.23	2.922	24.52 ^{+0.03} _{-0.03}	24.95 ^{+0.04} _{-0.04}	24.72 ^{+0.04} _{-0.04}
DSF2237B-MD38	22:39:35.49	+ 11:50:27.50	3.328	24.00 ^{+0.03} _{-0.03}	23.78 ^{+0.02} _{-0.02}	23.57 ^{+0.02} _{-0.02}
DSF2237B-MD60a	22:39:27.91	+ 11:53:00.23	3.141	27.25 ^{+0.12} _{-0.11}	27.04 ^{+0.08} _{-0.07}	26.68 ^{+0.07} _{-0.07}
DSF2237B-MD60b	22:39:27.90	+ 11:52:59.86	3.141	26.96 ^{+0.11} _{-0.10}	26.78 ^{+0.07} _{-0.07}	26.46 ^{+0.07} _{-0.06}
DSF2237B-MD60c	22:39:27.93	+ 11:52:59.65	3.141	24.97 ^{+0.05} _{-0.05}	25.00 ^{+0.04} _{-0.04}	24.73 ^{+0.04} _{-0.03}
Q0933-D16a	09:33:30.59	+ 28:44:53.54	3.047	27.17 ^{+0.06} _{-0.06}	27.03 ^{+0.06} _{-0.06}	26.83 ^{+0.07} _{-0.07}
Q0933-D16b	09:33:30.58	+ 28:44:53.58	...	25.90 ^{+0.05} _{-0.05}	25.04 ^{+0.02} _{-0.02}	24.88 ^{+0.03} _{-0.03}
Q0933-M23a	09:33:20.62	+ 28:46:54.76	...	25.66 ^{+0.06} _{-0.05}	24.99 ^{+0.03} _{-0.03}	24.93 ^{+0.05} _{-0.05}
Q0933-M23b	09:33:20.71	+ 28:46:54.70	3.289	26.77 ^{+0.09} _{-0.08}	27.57 ^{+0.21} _{-0.18}	27.11 ^{+0.22} _{-0.18}
Q0933-MD75	09:33:24.41	+ 28:47:46.24	2.913	25.21 ^{+0.03} _{-0.03}	25.76 ^{+0.05} _{-0.05}	25.70 ^{+0.08} _{-0.08}
Q0933-MD83	09:33:21.51	+ 28:48:46.70	2.880	25.42 ^{+0.06} _{-0.05}	25.20 ^{+0.05} _{-0.05}	24.88 ^{+0.06} _{-0.06}
Q1422-d42a	14:24:27.75	+ 22:53:51.01	3.137	25.47 ^{+0.05} _{-0.04}	25.56 ^{+0.05} _{-0.05}	25.45 ^{+0.06} _{-0.05}
Q1422-d42b	14:24:27.73	+ 22:53:50.84	3.137	26.04 ^{+0.05} _{-0.05}	26.29 ^{+0.07} _{-0.06}	26.07 ^{+0.07} _{-0.06}
Q1422-d57	14:24:43.25	+ 22:56:06.67	2.946	25.68 ^{+0.06} _{-0.06}	25.82 ^{+0.08} _{-0.07}	25.65 ^{+0.08} _{-0.07}
Q1422-d68a	14:24:32.92	+ 22:58:29.84	3.287	27.76 ^{+0.12} _{-0.11}	28.52 ^{+0.30} _{-0.23}	28.50 ^{+0.39} _{-0.29}
Q1422-d68b	14:24:32.94	+ 22:58:29.03	3.287	24.86 ^{+0.03} _{-0.03}	25.15 ^{+0.04} _{-0.04}	24.91 ^{+0.04} _{-0.04}
Q1422-d68c	14:24:32.98	+ 22:58:28.89	3.287	26.81 ^{+0.09} _{-0.08}	26.49 ^{+0.07} _{-0.07}	26.65 ^{+0.10} _{-0.09}
Q1549-C25	15:52:06.07	+ 19:11:28.44	3.153	24.55 ^{+0.02} _{-0.02}	24.86 ^{+0.03} _{-0.03}	24.68 ^{+0.04} _{-0.03}
Q1549-D3a	15:51:43.72	+ 19:09:12.50	2.937	24.65 ^{+0.02} _{-0.02}	24.91 ^{+0.03} _{-0.03}	24.67 ^{+0.04} _{-0.03}
Q1549-D3b	15:51:43.71	+ 19:09:12.36	2.937	24.96 ^{+0.02} _{-0.02}	25.24 ^{+0.03} _{-0.03}	24.87 ^{+0.03} _{-0.03}
Westphal-CC38	14:18:03.81	+ 52:29:07.23	3.073	24.82 ^{+0.03} _{-0.03}	24.43 ^{+0.04} _{-0.04}	24.04 ^{+0.04} _{-0.04}
Westphal-MM37	14:18:26.24	+ 52:29:45.03	3.421	24.60 ^{+0.02} _{-0.02}	24.31 ^{+0.02} _{-0.02}	24.17 ^{+0.02} _{-0.02}
Westphal-MMD45a	14:18:19.81	+ 52:27:09.45	2.936	25.64 ^{+0.04} _{-0.04}	25.54 ^{+0.05} _{-0.05}	25.04 ^{+0.04} _{-0.04}
Westphal-MMD45b	14:18:19.80	+ 52:27:08.77	2.936	26.16 ^{+0.05} _{-0.05}	26.18 ^{+0.07} _{-0.06}	25.96 ^{+0.08} _{-0.07}

^aThe field the object is located in, the object name, and a letter corresponding to the subcomponent in Fig. 3. A subcomponent label is omitted in the case of single-component morphology.

^bSystemic redshift from S18.

^cSystemic redshifts are omitted for components determined to be at low redshift based on their $V_{606}J_{125}H_{160}$ colours.

4.1 $V_{606}J_{125}H_{160}$ colour–colour diagram

In order to explore the validity of using the $V_{606}J_{125}H_{160}$ colour–colour diagram to predict foreground contamination, we examined the distribution of low- and high-redshift galaxies in $V_{606}J_{125}H_{160}$ colour–colour space using the photometric catalogs of the 3D-*HST* Survey (Brammer et al. 2012; Skelton et al. 2014). We first analysed galaxies with spectroscopically-confirmed redshifts in the redshift range of our KLCS *HST* sample, $2.75 < z_{\text{spec}} < 3.4$, as a proxy for uncontaminated $z \sim 3$ objects. We considered all galaxies with spectroscopic redshifts lower than our KLCS *HST* sample, $z_{\text{spec}} < 2.75$, as a representation of potential foreground contaminants. We display the low-redshift and $z \sim 3$ populations alongside our detection and non-detection subcomponents in $V_{606}J_{125}H_{160}$ colour–colour space in the upper right-hand panel of Fig. 4. Similar to the contaminant and $z \sim 3$ populations of M15, the low-redshift and $z \sim 3$ samples of 3D-*HST* fall in distinct regions of $V_{606}J_{125}H_{160}$ colour–colour space. By using the 3D-*HST* sample to examine where different redshift populations of galaxies lie, we can predict whether an individual component in our analysis is a low-redshift interloper or the $z \sim 3$ source measured by KLCS spectroscopy.

We adapted an empirical approach to rejecting low-redshift contamination in our sample of LyC detections using different 3D-*HST* redshift samples. Here, we used a sample of galaxies with either photometric or spectroscopic redshifts in 3D-*HST*, prioritizing spectroscopic redshifts if a galaxy had both. Including galaxies with

photometric redshift measurements better samples the $V_{606}J_{125}H_{160}$ dynamic range of our targets and is more complete than a spectroscopic sample weighted towards either UV selected galaxies (Steidel et al. 2003; Reddy et al. 2012) or those with strong rest-optical emission lines measured through the WFC3 grism (Bezanson et al. 2016; Momcheva et al. 2016). We again built ‘contaminant’ and ‘ $z \sim 3$ arcsec samples with the redshift ranges of $2.75 < z < 3.4$ and $z < 2.75$, respectively. These 3D-*HST* samples are shown with the KLCS *HST* subcomponents overlaid in the lower left-hand panel of Fig. 4. We translated these sample distributions into a quantitative, predictive model using the Gaussian kernel-density estimation (KDE) method (Parzen 1962; Rosenblatt 1956). This analysis assigns each $V_{606}J_{125}H_{160}$ data point a 2D Gaussian profile in colour–colour space. These Gaussians are summed together to estimate the underlying 2D PDF of the distribution of data points. This PDF can be used to estimate the likelihood that a random galaxy drawn from the sample would have a specific $V_{606}J_{125}H_{160}$. We constructed PDFs using the KDE method for our contaminant and $z \sim 3$ samples using the SCIPY routine *Gaussian_kde* with bandwidth determined by Scott’s Rule (Virtanen et al. 2020; Scott 2015). These PDFs are displayed in the lower right-hand panel of Fig. 4, each normalized to one.

We additionally examined the effects of the photometric errors of our measurements and the 3D-*HST* samples in the constructed PDFs. We generated 100 realizations of the 3D-*HST* contaminant and $z \sim 3$ samples randomly perturbed by their $V_{606}J_{125}H_{160}$ errors.

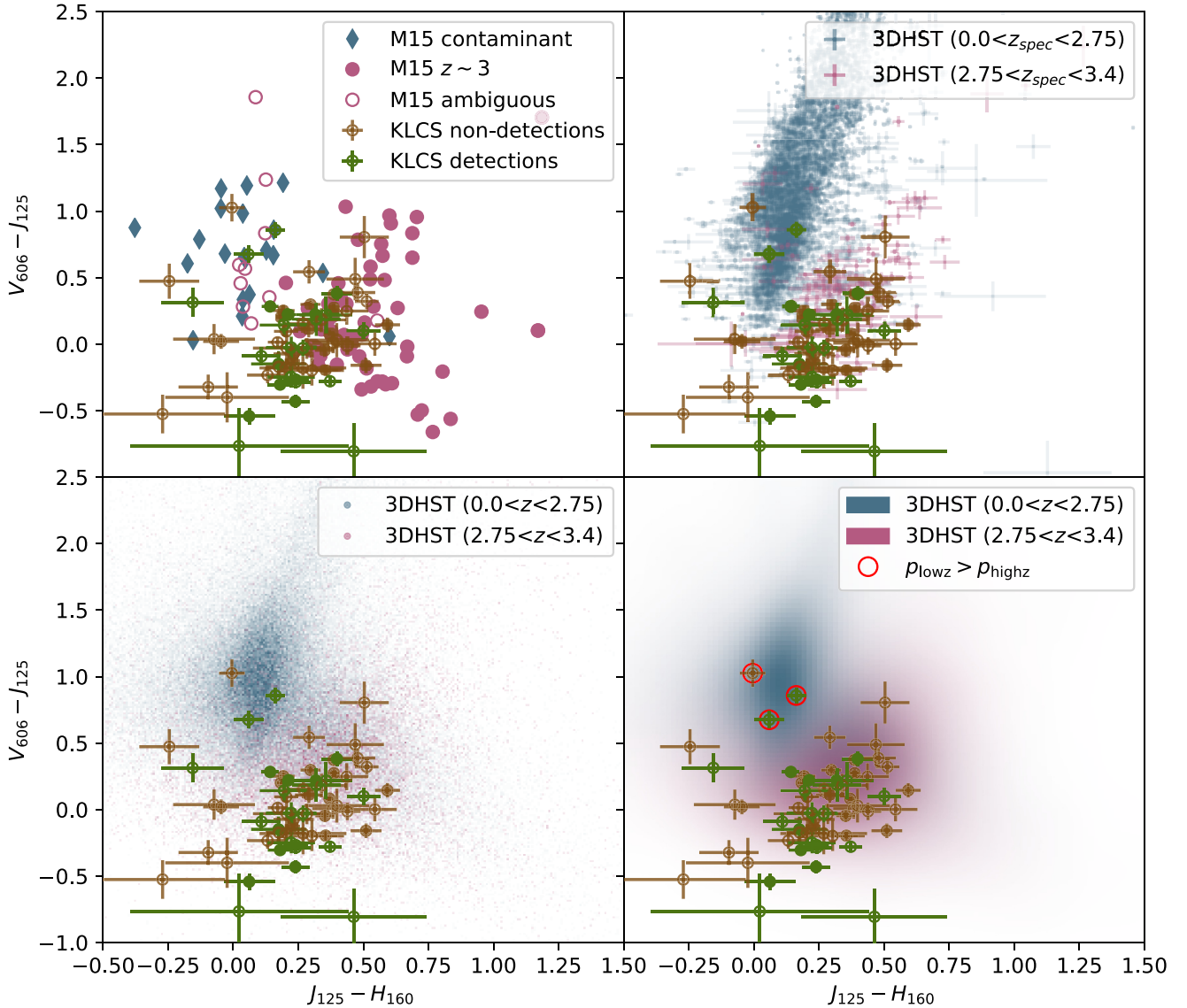


Figure 4. **Upper left:** $V_{606}J_{125}H_{160}$ colour–colour diagram of LyC detection candidates from M15. The contaminants, selected by photometric-redshift fitting, are displayed as blue diamonds. Subcomponents predicted at $z \sim 3$ are displayed as solid pink circles, while components with ambiguous SEDs are displayed as unfilled pink circles. Also displayed are all subcomponents extracted from the photometry of the KLCS *HST* sample, separated into LyC detections in green and non-detections in brown. Open circles represent subcomponents from multicomponent objects, while filled circles represent single-component objects. **Upper right:** The subcomponents of the KLCS *HST* sample overlaid with spectroscopic redshift samples of 3D-*HST*. The contaminant sample ($z_{\text{spec}} < 2.75$) is displayed in blue while the $z \sim 3$ ($2.75 < z_{\text{spec}} < 3.4$) sample is displayed in pink. **Lower left:** The subcomponents of the KLCS *HST* sample overlaid with photometric and spectroscopic redshift samples of 3D-*HST*. The redshift ranges of the two samples are identical to the spectroscopic redshift samples. Error bars of the 3D-*HST* samples are removed for clarity. **Lower right:** The subcomponents of the KLCS *HST* sample overlaid with the probability density functions (PDFs) estimated from the 3D-*HST* samples of the lower left-hand panel. Each PDF was constructed using the Gaussian KDE method and were normalized to one. Components of the LyC detections Q0933-M23 and Q1422-D16 and a component of the LyC non-detection Q1422-md145 can be seen in the peak region of the contaminant (blue) PDF and are highlighted in red.

We evaluated the resulting PDFs at the $V_{606}J_{125}H_{160}$ colours of our subcomponents, resulting in 100 probabilities from the contaminant and $z \sim 3$ PDFs for each component. We then took the median of these probabilities and compared them on a component-to-component basis. If the median likelihood drawn from the contaminant PDF was higher than that from the $z \sim 3$ PDF, the component was assigned as a contaminant. If the $z \sim 3$ median likelihood was higher, the component was confirmed to be at $z \sim 3$.

We found that two apparent LyC detections (Q0933-M23 and Q0933-D16) contained components that had a higher likelihood of

being drawn from the contaminant sample than the $z \sim 3$ sample. We also found one LyC non-detection (Q1422-md145) that was similarly consistent with being contaminated. As a sanity check, we examined the predictions of our targets that were least likely to be contaminated, the LyC non-detections with single-component morphology. All of these objects had components consistent with being at $z \sim 3$. We also examined the predictions from estimating PDFs only from 3D-*HST* galaxies with spectroscopically confirmed redshifts and found them to be consistent with predictions from the larger photometric-redshift 3D-*HST* samples.

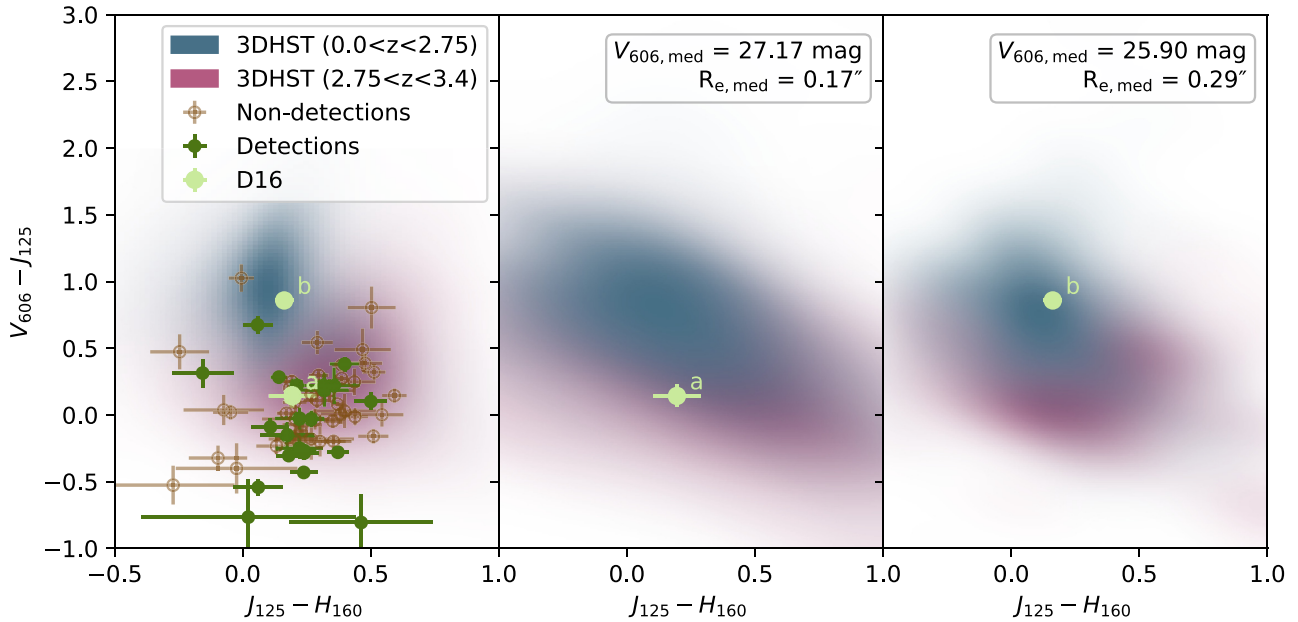


Figure 5. PDFs generated by the Gaussian KDE method on samples of 3D-*HST* galaxies at similar UV magnitudes and effective radii to Q0933-D16a and Q0933-D16b. **Left:** PDFs generated from the full 3D-*HST* redshift samples in $V_{606}J_{125}H_{160}$ colour–colour space. The Q0933-D16a and Q0933-D16b subcomponents are highlighted. **Middle and right:** PDFs generated from 3D-*HST* redshift samples with similar V_{606} apparent magnitude and effective radii as the subcomponents of Q0933-D16. The median V_{606} apparent magnitude and R_e are listed in the legend and are comparable to those of the components (see Table 1). The same redshift ranges as the left-hand panel were used for the low-redshift (blue) and $z \sim 3$ (pink) distributions.

Using the $V_{606}J_{125}H_{160}$ PDF estimated from Gaussian KDE to predict sample membership is built on a number of assumptions. By normalizing each PDF to one and comparing the probability values at a given $V_{606}J_{125}H_{160}$ directly, we assumed that each component has equal likelihood of being drawn from either distribution. We consider this assumption to be conservative, considering at least one component must be contributing spectroscopic signal consistent with $z \sim 3$, and the rigorous spectroscopic-blending rejection performed by S18.

We also assumed that the 3D-*HST* contaminant and $z \sim 3$ distributions we have constructed are representative of possible foreground contaminants and uncontaminated $z \sim 3$ KLCS galaxies. To examine this assumption, we constructed $V_{606}J_{125}H_{160}$ PDFs that were individually tailored to the properties of each component. For each subcomponent, a $z \sim 3$ and contaminant 3D-*HST* sample were constructed with galaxies of similar effective radii and V_{606} magnitude. 3D-*HST* effective radii measurements were drawn from Van Der Wel et al. (2012) with areas required to be within 2σ of the size of the SEXTRACTOR V_{606} isophotal area of the subcomponent, while V_{606} magnitudes were required to be within 1σ of the subcomponent V_{606} magnitude. These cuts, defined using the Van Der Wel et al. (2012) errors on effective radius and our photometric-error estimate of Section 3.2, were set to ensure that both the $z \sim 3$ and contaminant PDFs were well sampled. We bootstrapped the sample to generate median probability predictions in the method described above. The effects of cutting the 3D-*HST* samples based on effective radius and V_{606} magnitude are shown for the two-component object Q0933-D16 in Fig. 5. Here, we restricted the 3D-*HST* samples to have a median V_{606} magnitude of 27.17 mag and 25.90 mag and median effective radii of 0.17 arcsec and 0.29 arcsec for subcomponents *a* and *b*, motivated by the properties of the components. These cuts changed the shape

of the contaminant and $z \sim 3$ PDFs, but ultimately did not affect the classification of component *a* at $z \sim 3$ and component *b* as a contaminant. We found that the only object to be classified differently by this method was the non-detection Q1422-d53, now predicted to contain low-redshift components. We display the 3D-*HST* $z \sim 3$ and low-redshift PDFs after Q1422-d53 brightness and size cuts in Fig. 6. Using these modified PDFs, components *d*, *e*, and *f* were predicted to be low redshift. We considered this method to be more physically motivated and remove Q1422-d53 from the non-detection sample.

Finally, we consider the potential effects of contamination from $2.75 < z \leq 3.0$ interlopers of galaxies with spectroscopic redshifts at the high-redshift end of our sample ($3.0 < z < 3.4$). Out of the 13 individual LyC detection candidates remaining once Q0933-D16 and Q0933-M23 are removed, this type of contamination is relevant for the three multicomponent galaxies, DSF2237b-MD60, Q1422-d42, and Q1422-d68 (i.e. the other 10 galaxies are either single component or at $z < 3.0$). We rebuild the 3D-*HST* ‘contaminant’ sample to include higher-redshift galaxies, changing the redshift range to $z < (z_{\text{sys}} - 0.1)$, where z_{sys} is the systemic redshift of the LBG in question. Subsequently, the 3D-*HST* ‘ $z \sim 3$ ’ sample was modified to have a redshift range of $(z_{\text{sys}} - 0.1) < z < 3.4$. Using this method, we found no difference in the classification of subcomponents for DSF2237b-MD60, Q1422-d42, and Q1422-d68. Specifically, all subcomponent colours are consistent with being drawn from the $(z_{\text{sys}} - 0.1) < z < 3.4$ population.

In summary, we removed two apparent LyC detections (Q0933-D16 and Q0933-M23) and two LyC non-detections (Q1422-md145 and Q1422-d53) from the KLCS sample based on evidence of contamination from the $V_{606}J_{125}H_{160}$ colours of their morphological subcomponents.

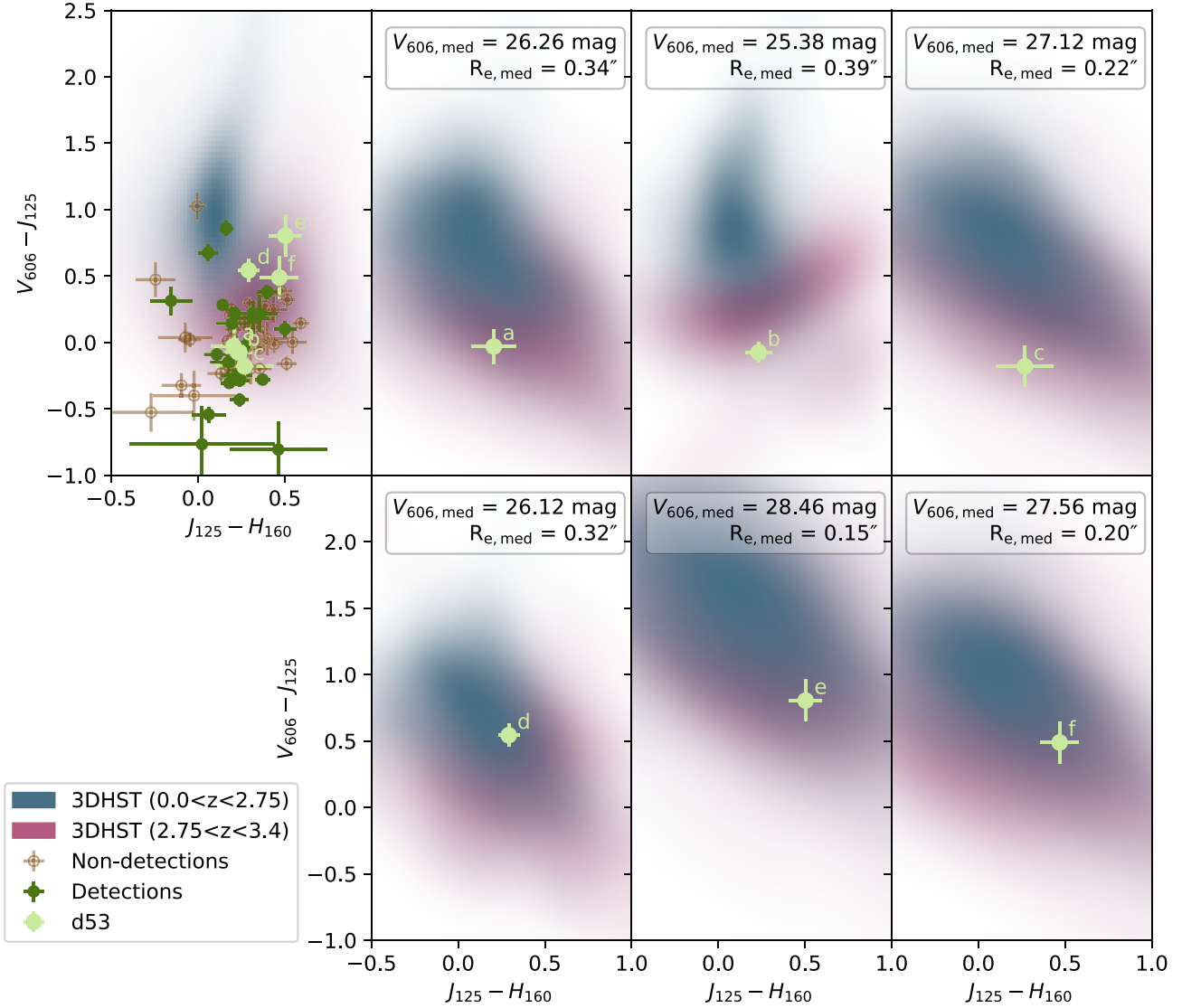


Figure 6. PDFs generated by the Gaussian KDE method on samples of 3D-*HST* galaxies at similar UV magnitudes and effective radii to the components of Q1422-d53. **Left:** PDFs generated from the full 3D-*HST* redshift samples in $V_{606}J_{125}H_{160}$ colour–colour space. The Q1422-d53 subcomponents are highlighted. Using these PDFs, all Q1422-d53 subcomponents are predicted at $z \sim 3$. **Right:** PDFs generated from 3D-*HST* redshift samples with similar V_{606} apparent magnitude and effective radii as the subcomponents of Q1422-d53. The median V_{606} apparent magnitude and R_e are listed in the legend and are comparable to those of the components (see Table A1). Components *d*, *e*, and *f* are predicted to be low redshift by these modified PDFs.

4.2 2D spectra

In addition to examining the positions of the KLCS *HST* components in $V_{606}J_{125}H_{160}$ colour–colour space, we analysed the high-resolution unsmoothed V_{606} images in tandem with the 2D LRIS spectra to search for new evidence of contamination. We examined the 2D spectra of the four objects predicted to be contaminated in Section 4.1. For Q0933-D16, Q1422-md145, and Q1422-d53, the subcomponents were either aligned along the slit or narrowly separated, making spectral deblending impossible. In Q0933-M23, we found evidence for foreground contamination in the LRIS spectrum shown in Fig. 7. Here, the Ly α feature used for spectroscopic redshift measurement is clearly offset from the continuum towards the component predicted to lie at $z \sim 3$ by our colour–colour method. There also exists an additional spectral feature offset toward the predicted low-redshift component that was classified as Ly α at $z = 3.380$ by S18. Based on the high-resolution photometric information offered by *HST* and the

lack of other offset spectral features, it is more likely this emission line is [O II] $\lambda 3727$ at $z = 0.43$.

5 RE-MEASUREMENT OF GLOBAL PROPERTIES

In this section, we revisit the results and conclusions of S18 with a $z \sim 3$ rest-UV spectroscopic sample free from significant foreground contamination in the LyC spectral range. With the removal of two apparent LyC detections, Q0933-D16 and Q0933-M23, whose emission is actually contaminated by lower-redshift interlopers, global properties of the sample will be unbiased by line-of-sight contamination and will present a more accurate picture of the global ionizing properties of galaxies in the $z \sim 3$ Universe. We also remove the LyC non-detections Q1422-md145 and Q1422-d53 due to evidence of low-redshift subcomponents within their *HST* morphology. Our rate of significant LyC detections for individual

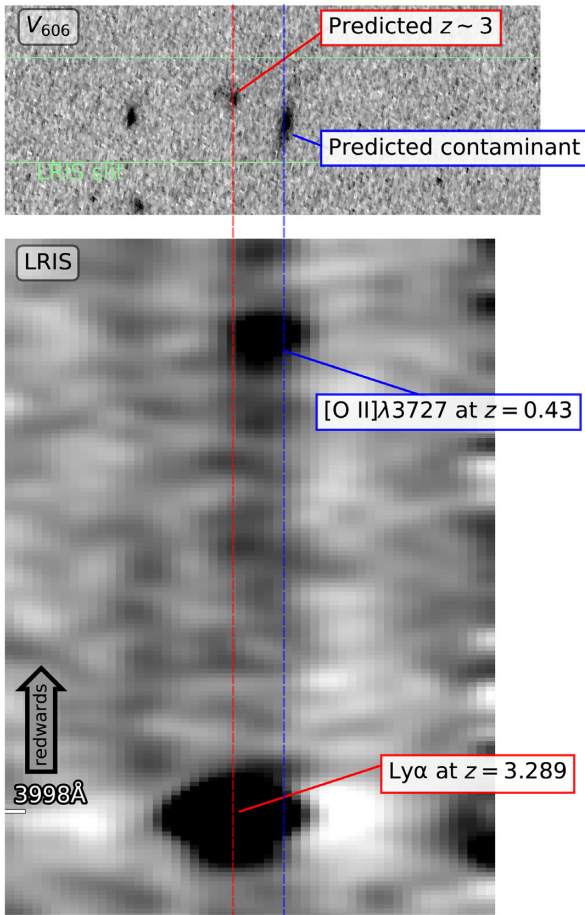


Figure 7. *HST* V_{606} imaging and LRIS spectrum of Q0933-M23. **Top:** Unsmoothed V_{606} postage stamp of Q0933-M23. The two components in the center of the image are associated with the extracted 1D spectrum of Q0933-M23. Color-colour analysis indicates that the left component, labeled in red, is at $z \sim 3$, while the right component is found to be a low-redshift interloper. Displayed in light green is the location of the LRIS slit that covered this source. **Bottom:** 2D LRIS spectrum of Q0933-M23 oriented such that wavelength increases upwards. The horizontal position has been matched with the top panel. In the center, the blended continuum for Q0933-M23 is shown, complete with the horizontal positions of the $z \sim 3$ and low-redshift component in dashed lines. The brighter $z = 3.289$ Ly α feature is offset towards the $z \sim 3$ component, while a spurious feature is offset towards the low-redshift component. The continuum to the left is from an unrelated object.

objects ($f_{900} > 3\sigma_{900}$) has been modified from 15/124 in S18 to 13/124 in this work, with a foreground contamination rate of 2/15 for galaxies with individual apparent LyC detections. We detail how the removal of these contaminated objects affects sample-averaged measurements of $\langle f_{900}/f_{1500} \rangle_{\text{out}}$ and $f_{\text{esc, abs}}$ as well as relationships between $\langle f_{900}/f_{1500} \rangle_{\text{out}}$, $f_{\text{esc, abs}}$ and galaxy properties. We also explore the change in ionizing emissivity in light of the cleaned sample.

Save for a small modification to the calculation of the ionizing emissivity, the methods in this section are identical to those of S18.

5.1 $\langle f_{900}/f_{1500} \rangle_{\text{out}}$

First, we analyse the ratio of ionizing to non-ionizing UV flux density in the uncontaminated KLCS sample. Following S18, in order to average out variations of IGM transmission in different sightlines

across the sky, we build a composite spectrum from the rest-frame, f_{1500} -normalized spectra of the sample, where f_{1500} is the average flux density in the range 1475–1525 Å. We combine the spectra using a spline-interpolated common wavelength grid, computing the mean flux density at each wavelength increment after 3σ rejection of outlier flux densities.

The ratio $\langle f_{900}/f_{1500} \rangle_{\text{obs}}$ is defined as the average observed flux density of the composite spectrum in the range 880–910 Å, f_{900} , divided by f_{1500} , both in units of $\text{erg s}^{-1} \text{cm}^{-2} \text{Hz}^{-1}$. Based on our cleaned sample of 120 galaxies, we estimate $\langle f_{900}/f_{1500} \rangle_{\text{obs}} = 0.015 \pm 0.002$, which is lower than the value of $\langle f_{900}/f_{1500} \rangle_{\text{obs}} = 0.019 \pm 0.002$ in S18. However, since f_{900} is heavily influenced by IGM and CGM transmission at $z \sim 3$, we perform transmission simulations required to estimate the ratio of ionizing to non-ionizing flux density directly outside the galaxy’s ‘LyC photosphere’ at $r_{\text{gal}} = 50$ (proper) kpc. This corrected ratio is defined as $\langle f_{900}/f_{1500} \rangle_{\text{out}}$. We generate 1000 estimates of t_{900} , the IGM + CGM transmission at 880–910 Å, where each simulation comprises 120 sightlines that have an identical redshift distribution to that of our sample. We then divide $\langle f_{900}/f_{1500} \rangle_{\text{obs}}$ by the average IGM + CGM transmission in the LyC region, $\langle t_{900} \rangle$, to obtain $\langle f_{900}/f_{1500} \rangle_{\text{out}}$, whose uncertainty includes the uncertainty in $\langle t_{900} \rangle$. We calculate $\langle f_{900}/f_{1500} \rangle_{\text{out}} = 0.040 \pm 0.006$ for the uncontaminated KLCS sample, compared to the ratio of $\langle f_{900}/f_{1500} \rangle_{\text{out}} = 0.057 \pm 0.006$ presented in S18. This ~ 30 per cent discrepancy represents the level of contamination introduced by the strong ~ 3500 Å flux density of low-redshift interlopers in Q0933-D16 and Q0933-M23, masquerading as rest-frame LyC emission at $z \sim 3$.

HST images are available only for the 24 LyC non-detections that lie on the pointings designed to target the apparent detection sample, thus we attempt to model the effects of potential contamination within the 85 KLCS non-detections without *HST* imaging. We build two composite spectra. The first contains the original 24 LyC non-detections imaged by *HST*. The second removes the two galaxies with low-redshift subcomponents, Q1422-md145 and Q1422-d53, for an uncontaminated *HST* non-detection sample of 22 galaxies. We then re-measure $\langle f_{900}/f_{1500} \rangle_{\text{out}}$ from sample composite spectra in order to analyse any bias in f_{900} that may arise from contamination in the full non-detection sample. We measure $\langle f_{900}/f_{1500} \rangle_{\text{out}}$ of the original non-detection *HST* sample and the uncontaminated non-detection *HST* sample to be 0.003 ± 0.006 and 0.002 ± 0.006 , respectively. Due to the lack of significant bias in $\langle f_{900}/f_{1500} \rangle_{\text{out}}$ from the inclusion of non-detections with low-redshift subcomponents, we conclude that the lack of *HST* imaging for the larger KLCS non-detection sample will not significantly bias our global measurements of LyC flux density. Nevertheless, a larger sample of non-detections with *HST* imaging will better quantify the level of contamination in the full sample.

We build additional composites to examine how LyC leakage correlates with a variety of galaxy properties. In addition to our full-sample composite of 120 galaxies (‘All’), we build a composite with the 13 galaxies with significant f_{900} (‘All, detected’) and a composite with the 107 galaxies with f_{900} non-detections (‘All, not detected’). We split the KLCS sample into four equivalent bins of increasing Ly α equivalent width ($W_{\lambda}(\text{Ly}\alpha)$ (Q1-Q4)) and decreasing UV luminosity (L_{UV} (Q1-Q4)). Each of these composites includes 120/4 = 30 galaxies, ensuring that the uncertainty due to variation in $\langle t_{900} \rangle$ is only ~ 10 per cent (see discussion in S18). We also construct composites by bisecting the sample at $W_{\lambda}(\text{Ly}\alpha)=0$ and $L_{\text{UV}} = L_{\text{UV}}^*$ ($M_{\text{UV}} = -21.0$; Reddy & Steidel 2009) to create ‘ $W_{\lambda}(\text{Ly}\alpha)>0$,’ ‘ $W_{\lambda}(\text{Ly}\alpha)<0$,’ ‘ $L_{\text{UV}} < L_{\text{UV}}^*$,’ and ‘ $L_{\text{UV}} > L_{\text{UV}}^*$.’ These composites, as well as all other composites defined by S18, are reconstructed based on our cleaned sample and corrected for IGM and CGM

transmission in the same manner as ‘All.’ We present the $\langle f_{900}/f_{1500} \rangle_{\text{out}}$ measurements for these composites in Table 2 along with the corresponding values from S18 for comparison.

5.2 Trends with $W_\lambda(\text{Ly}\alpha)$ and L_{UV}

A deep uncontaminated spectroscopic sample covering the LyC at $z \sim 3$ presents a unique opportunity to study how LyC leakage correlates with galaxy properties. This type of analysis is vital for understanding the physics of LyC escape and inferring a population of LyC leakers in the epoch of reionization.

We re-examine the galaxy characteristics most strongly associated with $\langle f_{900}/f_{1500} \rangle_{\text{out}}$ from S18: $W_\lambda(\text{Ly}\alpha)$ and L_{UV} . In S18, a strong correlation between $\langle f_{900}/f_{1500} \rangle_{\text{out}}$ and $W_\lambda(\text{Ly}\alpha)$ was measured in the KLCS sample using composite spectra in bins of $W_\lambda(\text{Ly}\alpha)$. In a similar manner, a strong anticorrelation between $\langle f_{900}/f_{1500} \rangle_{\text{out}}$ and L_{UV} was measured. We re-evaluate these trends using uncontaminated composites binned with respect to $W_\lambda(\text{Ly}\alpha)$ and L_{UV} and present them in Fig. 8 alongside a measurement from the ‘All’ composite. We recover the trends of increasing $\langle f_{900}/f_{1500} \rangle_{\text{out}}$ with lower L_{UV} and larger $W_\lambda(\text{Ly}\alpha)$ of S18, although the slopes are slightly shallower with the removal of contaminants with strong apparent f_{900} . We quantify this change in $\langle f_{900}/f_{1500} \rangle_{\text{out}}$ versus $W_\lambda(\text{Ly}\alpha)$ by performing a linear fit to the values of $\langle f_{900}/f_{1500} \rangle_{\text{out}}$ in the four independent quartiles of $W_\lambda(\text{Ly}\alpha)$, with the assumption that $\langle f_{900}/f_{1500} \rangle_{\text{out}}$ tends to zero at $W_\lambda(\text{Ly}\alpha)=0$. With the cleaned sample, we find

$$\langle f_{900}/f_{1500} \rangle_{\text{out}} = 0.28(W_{\text{Ly}\alpha}/110 \text{ \AA}), \quad (1)$$

which has a shallower slope than in the relationship $\langle f_{900}/f_{1500} \rangle_{\text{out}} \sim 0.36(W_{\text{Ly}\alpha}/110 \text{ \AA})$ presented in S18.

These correlations imply that LyC escape occurs in galaxies with $L_{\text{UV}} < L_{\text{UV}}^*$ and strong observed Ly α emission relative to their UV continuum. While both relationships are compelling, we note that $W_\lambda(\text{Ly}\alpha)$ transmission has been found to be a strong function of the H I covering fraction, both in the local Universe and at $z \sim 3$ (e.g. Reddy et al. 2016; Gazagnes et al. 2018). To deepen our physical picture of a LyC leaking galaxy, we must consider descriptions of the structure of the neutral-phase ISM.

5.3 $f_{\text{esc, abs}}$

While $\langle f_{900}/f_{1500} \rangle_{\text{out}}$ is a particularly effective observational parameter for informing the global ionizing budget using only the observed FUV luminosity function (LF) at high redshift (e.g. S18; Ouchi et al. 2009), it is also important to understand how ionizing radiation escapes galaxies in relation to their intrinsic SFRs. To this end, we must simultaneously model the intrinsic UV stellar spectrum as well as the H I and dust in the ISM that these photons encounter. All of these factors are required to describe the absolute escape fraction ($f_{\text{esc, abs}}$), defined here as the ratio of escaping LyC photons to those produced by stars for the assumed stellar-population synthesis (SPS) model.

We estimate $f_{\text{esc, abs}}$ in the uncontaminated KLCS composites using SPS model fits to the IGM + CGM-corrected composite spectra. We use identical SPS models to those in S18 (also see Steidel et al. 2016), with stellar metallicity $Z_* = 0.001$, IMF slope $\alpha = -2.35$, and upper stellar mass limit of $300 M_\odot$ from BPASS (BPASS v2.1; Eldridge et al. 2017). We also assume a continuous star-formation history and an age of $t = 10^8$ yr. We allow the continuum reddening to vary across $0 \leq E(B - V) < 1.0$ for a variety of attenuation relations

(Reddy et al. 2015, 2016; Gordon et al. 2003). We simultaneously perform geometric ISM modeling for each composite, quantifying the covering fraction (f_c) of the optically thick H I gas attenuating the FUV continuum. We adopt the ‘holes’ model of S18 to describe the physical arrangement of H I and dust around the H II regions of our galaxies, where neutral H I exists in a picket-fence configuration and dust is only located where neutral gas is (also see Reddy et al. 2016). Accordingly, f_c varies between zero and one and the ‘holes’ are free of both H I and dust. This model is consistent with correlations found between Ly α emission strength and low-ionization interstellar absorption strength in star-forming galaxies at intermediate redshifts (Shapley et al. 2003; Steidel et al. 2010; Du et al. 2018; Pahl et al. 2020). S18 defines the attenuated observed spectrum as

$$S_{v, \text{obs}} = S_{v, \text{int}} \left[(1 - f_c) + f_c e^{-\tau(\lambda)} 10^{-A_\lambda/2.5} \right], \quad (2)$$

where $S_{v, \text{int}}$ is the intrinsic stellar spectrum, $A_\lambda = k_\lambda(E(B - V)_{\text{cov}})$ where $E(B - V)_{\text{cov}}$ is the continuum reddening in the foreground gas (and k_λ is the wavelength-dependent dust attenuation law), and $e^{-\tau(\lambda)}$ is the transmission function due to line and continuum absorption (a function of H I column density $N_{\text{H I}}$).

We fit for $E(B - V)_{\text{cov}}$, $\log(N_{\text{H I}})$ (cm^{-2}), and f_c for each composite and tabulate the results in Table 3. In the ‘holes’ model, the H I and dust are optically thick to ionizing light save for the holes in the ISM where extreme UV light is transmitted entirely. Thus, the relation between $f_{\text{esc, abs}}$ and f_c in this ISM model is simply

$$f_{\text{esc, abs}} = 1 - f_c. \quad (3)$$

We list the estimated $f_{\text{esc, abs}}$ for each composite in Table 3 along with the values from S18 for comparison.

A key result from this analysis is the sample-averaged $f_{\text{esc, abs}}$ of the KLCS survey. Based on the ‘All’ composite, we estimate $f_{\text{esc, abs}} = 0.06 \pm 0.01$, lower than the sample-averaged $f_{\text{esc, abs}} = 0.09 \pm 0.01$ of S18. The value of $f_{\text{esc, abs}}$ is an essential input to models of the contribution of star-forming galaxies to reionization. Due to increased attenuation from the neutral-phase IGM at $z > 3$, observing this quantity at higher redshifts becomes increasingly difficult (Vanzella et al. 2012; S18). Well-constrained direct measurements of model-independent $\langle f_{900}/f_{1500} \rangle_{\text{out}}$ and model-dependent $f_{\text{esc, abs}}$ at $z \sim 3$ inform our picture of LyC escape at high redshift and have direct consequences for the contribution of star-forming galaxies to the ionizing background. Foreground contamination in only two galaxies in a sample of 124 can elevate $f_{\text{esc, abs}}$ by ~ 30 per cent, underlining the need for high-resolution, multiband imaging of LyC detection candidates at $z \sim 3$ to vet sample-averaged measurements (Vanzella et al. 2012; M15).

We emphasize that $f_{\text{esc, abs}}$ is calculated here relative to BPASS SPS models that are characterized by a high ionizing photon production efficiency ($\xi_{\text{ion}} = 25.5$). If we instead, for example, assume an SPS model with $\xi_{\text{ion}} = 25.2$ (e.g. Robertson et al. 2013, 2015) we would infer $f_{\text{esc, abs}}$ a factor of \sim two larger for our full sample composite. In contrast, $\langle f_{900}/f_{1500} \rangle_{\text{out}}$ is a (mostly) model-independent measure of escaping ionizing radiation that only depends on a mean IGM + CGM correction, and does not rely on assumptions about the underlying stellar population, including stellar age.

We again connect our composite measurements of LyC escape with galaxy characteristics, now in terms of the relationship between $f_{\text{esc, abs}}$ and $W_\lambda(\text{Ly}\alpha)$ within the uncontaminated KLCS sample. We display the $f_{\text{esc, abs}}$ and $W_\lambda(\text{Ly}\alpha)$ measurements for each composite in Fig. 9, including 2σ upper limits for measurements with less than 2σ significance. We highlight the four independent quartiles of $W_\lambda(\text{Ly}\alpha)$

Table 2. $\langle f_{900}/f_{1500} \rangle_{\text{out}}$ measurements of KLCS composite spectra after contamination removal.

Sample ^a	$\langle f_{900}/f_{1500} \rangle_{\text{out}}$ (S18)	$\langle f_{900}/f_{1500} \rangle_{\text{out}}$ (this work)
All	0.057 ± 0.006	0.040 ± 0.006
All, detected ^b
All, not detected ^b
$W_\lambda(\text{Ly}\alpha) > 0$	0.086 ± 0.010	0.063 ± 0.009
$W_\lambda(\text{Ly}\alpha) < 0$	0.019 ± 0.008	0.016 ± 0.011
LAEs	0.175 ± 0.026	0.107 ± 0.023
Non-LAEs	0.032 ± 0.008	0.030 ± 0.008
$L_{UV} > L_{UV}^*$	0.006 ± 0.008	0.005 ± 0.008
$L_{UV} < L_{UV}^*$	0.113 ± 0.014	0.085 ± 0.012
L_{UV} (Q1)	0.005 ± 0.008	0.011 ± 0.008
L_{UV} (Q2)	0.000 ± 0.011	0.000 ± 0.006
L_{UV} (Q3)	0.114 ± 0.018	0.075 ± 0.016
L_{UV} (Q4)	0.138 ± 0.024	0.111 ± 0.022
z (Q1)	0.053 ± 0.018	0.050 ± 0.018
z (Q4)	0.056 ± 0.011	0.050 ± 0.014
$W_\lambda(\text{Ly}\alpha)$ (Q1)	0.013 ± 0.011	0.005 ± 0.010
$W_\lambda(\text{Ly}\alpha)$ (Q2)	0.033 ± 0.011	0.048 ± 0.014
$W_\lambda(\text{Ly}\alpha)$ (Q3)	0.047 ± 0.015	0.033 ± 0.014
$W_\lambda(\text{Ly}\alpha)$ (Q4)	0.166 ± 0.025	0.103 ± 0.020
$(G - R)_0$ (Q1)	0.055 ± 0.013	0.050 ± 0.012
$(G - R)_0$ (Q2)	0.059 ± 0.017	0.032 ± 0.016
$(G - R)_0$ (Q3)	0.080 ± 0.016	0.089 ± 0.017
$(G - R)_0$ (Q4)	0.029 ± 0.016	0.000 ± 0.013

^aFull composite descriptions can be found in S18.

^bDue to the uncertainty in the IGM + CGM correction, these entries are omitted.

in black and fit a linear trend to these points, fixing $f_{\text{esc, abs}} = 0$ at $W_\lambda(\text{Ly}\alpha) = 0$, and treating the upper limits as $f_{\text{esc, abs}} = 0$ with the appropriate Gaussian error. We recover the relationship

$$f_{\text{esc, abs}} = 0.58(W_{\text{Ly}\alpha}/110\text{\AA}), \quad (4)$$

slightly shallower than $f_{\text{esc, abs}} = 0.75(W_{\text{Ly}\alpha}/110\text{\AA})$ as presented in S18. This relationship between $f_{\text{esc, abs}}$ and $W_\lambda(\text{Ly}\alpha)$ supports the assertion that the escape of LyC photons is directly connected with the spatially-resolved distribution of H I in the ISM that governs $W_\lambda(\text{Ly}\alpha)$ measurements at $z \sim 3$ (e.g. Scarlata et al. 2009; Rivera-Thorsen et al. 2015). Similar relationships between $f_{\text{esc, abs}}$ and $W_\lambda(\text{Ly}\alpha)$ have been found in other large-scale LyC surveys at $z \sim 3-4$ (Marchi et al. 2017, 2018; Fletcher et al. 2019). f_c and Ly α escape fraction have also been determined to predict LyC escape fractions at low redshift (Chisholm et al. 2018; Gazagnes et al. 2018). Additionally, *HST* analysis of a spatially resolved FUV colour map has shown that bluer colours are coincident with LyC escape, demonstrating that favorable H I and dust configurations lead to LyC escape (Ji et al. 2020). Finally, the Ly α kinematics of a strongly-leaking $z \sim 3$ galaxy have demonstrated the consistent geometry of LyC and Ly α escape (Vanzella et al. 2020).

5.4 Ionizing emissivity and implications

The removal of apparent LyC leakers with evidence of foreground contamination has lowered our estimates of $\langle f_{900}/f_{1500} \rangle_{\text{out}}$ and $f_{\text{esc, abs}}$ compared to previous values based on the composites of S18. Additionally, the relationships between $\langle f_{900}/f_{1500} \rangle_{\text{out}}$ and L_{UV} , $\langle f_{900}/f_{1500} \rangle_{\text{out}}$ and $W_\lambda(\text{Ly}\alpha)$, and $f_{\text{esc, abs}}$ and $W_\lambda(\text{Ly}\alpha)$ have been recovered, but with slightly shallower correlation slopes.

We explore the effects of these updated results on the predictions of the galactic contributions to the ionizing background at $z \sim 3$ by re-tracing the global emissivity calculations of (S18). The ionizing

emissivity of galaxies can be estimated by

$$\epsilon_{\text{LyC}} \simeq \int_{L_{UV, \text{min}}}^{L_{UV, \text{max}}} \langle f_{900}/f_{1500} \rangle_{\text{out}}(L_{UV}) \times L_{UV} \Phi(L_{UV}) dL_{UV}, \quad (5)$$

where $\Phi(L_{UV})$ is the galaxy LF evaluated in the rest-frame FUV (1500–1700 Å). We can perform a simple estimate by expressing $\langle f_{900}/f_{1500} \rangle_{\text{out}}$ as a function of L_{UV} , taking $\langle f_{900}/f_{1500} \rangle_{\text{out}} = 0$ for galaxies with $M_{UV} \leq -21.0$ and $\langle f_{900}/f_{1500} \rangle_{\text{out}} = 0.085$ for galaxies with $-21 < M_{UV} \leq -19.5$ (see ‘ $L_{UV} < L_{UV}^*$ ’ and ‘ $L_{UV} > L_{UV}^*$ ’ composites in Table 2). Using the UV LF from Reddy & Steidel (2009), we calculate a corrected $\epsilon_{\text{LyC}} \simeq 9.78 \times 10^{24} \text{ erg s}^{-1} \text{ Hz}^{-1} \text{ Mpc}^{-3}$, compared to the S18 value of $\epsilon_{\text{LyC}} \simeq 13.0 \times 10^{24} \text{ erg s}^{-1} \text{ Hz}^{-1} \text{ Mpc}^{-3}$.

As in S18, we examine an alternate estimate of the ionizing emissivity by assuming that $\langle f_{900}/f_{1500} \rangle_{\text{out}}$ varies with $W_\lambda(\text{Ly}\alpha)$. This estimation is supported by the strong relationship between the two properties in Fig. 8 and can be extrapolated to higher redshifts if $W_\lambda(\text{Ly}\alpha)$ is corrected for IGM opacity. For this calculation, we move $\langle f_{900}/f_{1500} \rangle_{\text{out}}$ outside the integral in equation (5), and estimate an average $\langle f_{900}/f_{1500} \rangle_{\text{out}}$ weighted by $W_\lambda(\text{Ly}\alpha)$. We multiply this average $\langle f_{900}/f_{1500} \rangle_{\text{out}}$, $E(\langle f_{900}/f_{1500} \rangle_{\text{out}})$, by the integral over the non-ionizing UV LF, ϵ_{UV} . To find the $W_\lambda(\text{Ly}\alpha)$ -weighted average value of $\langle f_{900}/f_{1500} \rangle_{\text{out}}$, we combine our relationships between $\langle f_{900}/f_{1500} \rangle_{\text{out}}$ and $W_\lambda(\text{Ly}\alpha)$ in equation (1) and the distribution function $n(W_\lambda(\text{Ly}\alpha))$.

While it is possible to combine equation (1) and $n(W_\lambda(\text{Ly}\alpha))$ directly, we introduce physical descriptions of Ly α escape to extrapolate the behaviour of $\langle f_{900}/f_{1500} \rangle_{\text{out}}$ outside of the range of $W_\lambda(\text{Ly}\alpha)$ in our sample. S18 connected the modulation of $W_\lambda(\text{Ly}\alpha)$ by f_c through two separate processes: the scattering of Ly α photons by foreground gas and the decrease in the Ly α source function when H II regions are no longer optically thick to ionizing radiation. These processes

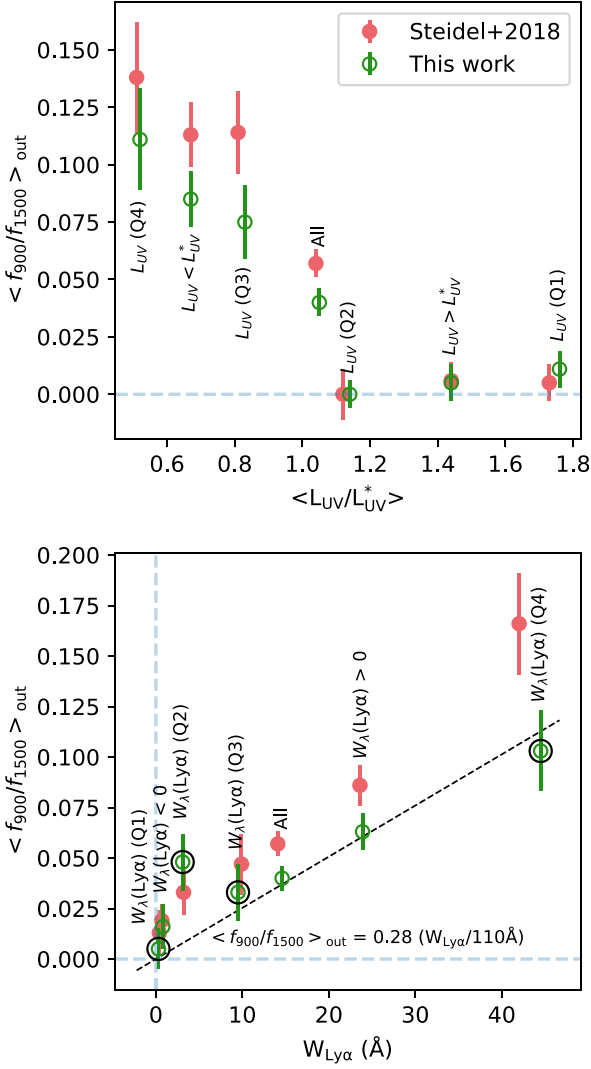


Figure 8. Trends of $\langle f_{900}/f_{1500} \rangle_{\text{out}}$ as a function of L_{UV} and $W_{\lambda}(\text{Ly}\alpha)$ from KLCs composites. **S18** composite measurements are shown with solid red circles, while updated measurements from this work are shown with open green circles. **Top:** Composites in bins of L_{UV} , including four in independent quartiles of L_{UV} and two bisecting the sample on L_{UV}^* . Also displayed is the full-sample composite, ‘All.’ A decreasing almost-bimodal relationship is seen preserved between $\langle f_{900}/f_{1500} \rangle_{\text{out}}$ and L_{UV} . **Bottom:** Composites in bins of $W_{\lambda}(\text{Ly}\alpha)$, including four independent quartiles of $W_{\lambda}(\text{Ly}\alpha)$ and two bisecting the sample on $W_{\lambda}(\text{Ly}\alpha) = 0$, and the ‘All’ composite. Also displayed is the increasing linear fit to the four independent quartiles that are highlighted with black circles.

connect through the equation

$$(1 - f_c) = 0.5 - [0.5W' - 0.25]^{1/2}, \quad (6)$$

where $W' \equiv W_{\lambda}(\text{Ly}\alpha)/W_{\lambda}(\text{Ly}\alpha, \text{Case B})$ and $W_{\lambda}(\text{Ly}\alpha, \text{Case B}) = 110 \text{ \AA}$ in our assumed SPS model. We can join this physically motivated parameterization with the empirical relations in equations (1) and (4) to express $\langle f_{900}/f_{1500} \rangle_{\text{out}}$ in terms of W' ,

$$\langle f_{900}/f_{1500} \rangle_{\text{out}} \sim 0.24 - [0.117W' - 0.058]^{1/2}. \quad (7)$$

To calculate the expectation value of $\langle f_{900}/f_{1500} \rangle_{\text{out}}$ weighted by W' , we now include the relative incidence of $W_{\lambda}(\text{Ly}\alpha)$,

$$n(W_{\lambda}) \propto \exp(-W_{\lambda}/23.5\text{\AA}), \quad (8)$$

consistent with **S18** and spectroscopic samples analysed in Shapley et al. (2003) and Kornei et al. (2010). To find the expectation value of $\langle f_{900}/f_{1500} \rangle_{\text{out}}$, $E(\langle f_{900}/f_{1500} \rangle_{\text{out}})$, we simplify the method of **S18** by integrating equation (8) with a change of variables from equation (7). After including an assumption that 40 per cent of galaxies have $W_{\lambda}(\text{Ly}\alpha) \leq 0$ and therefore $\langle f_{900}/f_{1500} \rangle_{\text{out}} \simeq 0$ for such sources, we find that the integral becomes

$$E(\langle f_{900}/f_{1500} \rangle_{\text{out}}) = \frac{0.6 \int_0^1 [0.24 - [0.117W' - 0.058]^{1/2}] \times \exp(-W' \times (110/23.5)) dW'}{\int_0^1 \exp(-W' \times (110/23.5)) dW'} \quad (9)$$

and evaluates to $E(\langle f_{900}/f_{1500} \rangle_{\text{out}}) = 0.032$. Based on the equivalent values relating $\langle f_{900}/f_{1500} \rangle_{\text{out}}$, $f_{\text{esc,abs}}$, and $W_{\lambda}(\text{Ly}\alpha)$ from **S18**, this method estimates $E(\langle f_{900}/f_{1500} \rangle_{\text{out}}) = 0.042$. We then multiply $E(\langle f_{900}/f_{1500} \rangle_{\text{out}})$ by ϵ_{UV} to find $\epsilon_{\text{LyC}} \simeq 5.5 \times 10^{24} \text{ erg s}^{-1} \text{ Hz}^{-1} \text{ Mpc}^{-3}$. For comparison, when we apply this methodology to the contaminated **S18** results, we find a higher emissivity of $\epsilon_{\text{LyC}} \simeq 7.2 \times 10^{24} \text{ erg s}^{-1} \text{ Hz}^{-1} \text{ Mpc}^{-3}$. Our value remains consistent with other recent estimates, such as those in Jones, Barger & Cowie (2021): $\epsilon_{\text{LyC}} \simeq 10.0^{+10.0}_{-5.0} \times 10^{24} \text{ erg s}^{-1} \text{ Hz}^{-1} \text{ Mpc}^{-3}$ at $z \sim 2.5$ and $\epsilon_{\text{LyC}} \simeq 15.8^{+34.3}_{-10.8} \times 10^{24} \text{ erg s}^{-1} \text{ Hz}^{-1} \text{ Mpc}^{-3}$ at $z \sim 2.9$.

The reduction of ionizing emissivity from star-forming galaxies found using the uncontaminated composites of this work is significant. However, galaxies still provide a comparable contribution to the ionizing background at $z \sim 3$ to that of active galactic nuclei (AGNs) that are estimated to contribute between 1.6 and $10 \times 10^{24} \text{ erg s}^{-1} \text{ Hz}^{-1} \text{ Mpc}^{-3}$ at these redshifts (Hopkins, Richards & Hernquist 2007; Cowie, Barger & Trouille 2009; Kulkarni, Worseck & Hennawi 2019; Shen et al. 2020). Furthermore, the unique size, purity, and data products of the sample in this work can inform the details of reionization models and the physics of LyC escape at $z > 3$. Authors have recently described competing models of reionization as ‘democratic,’ where reionization is driven by numerous faint sources with high $f_{\text{esc,abs}}$ (e.g. Finkelstein et al. 2019), and ‘oligarchical,’ where <5 per cent of galaxies contribute >80 per cent of the reionization budget (Naidu et al. 2020). Both of these interpretations depend on base assumptions of the evolution and value of $f_{\text{esc,abs}}$ across cosmic time and the degree of LyC leakage associated with a range of galaxy properties.

Finkelstein et al. (2019) used a halo-mass-dependent $f_{\text{esc,abs}}$ in their fiducial model. These authors also considered a fixed $f_{\text{esc,abs}} = 0.09 \pm 0.01$, as found in **S18**, and accordingly report tension with observational constraints on the progress of reionization. However, in order to consider the implications of different $f_{\text{esc,abs}}$ values on the evolution of the ionizing emissivity, careful attention must be paid to the manner in which key quantities are empirically estimated, modeled, or assumed. Given that the most robust quantity we estimate is $\langle f_{900}/f_{1500} \rangle_{\text{out}}$, the only fair way to incorporate our $f_{\text{esc,abs}}$ value into the Finkelstein et al. (2019) model is also to assume the same intrinsic LyC luminosity for similar galaxies. Additionally, the fiducial model of Finkelstein et al. (2019) predicts that AGNs dominate the ionizing budget even extrapolated to $z \sim 3$, a determination in tension with this work and **S18**. Keeping in mind the same caveats about incorporating an $f_{\text{esc,abs}}$ determined from observations into reionization models, we turn to Naidu et al. (2020), who built two empirical models, one that fits for a constant $f_{\text{esc,abs}} = 0.21^{+0.06}_{-0.04}$ during reionization and one that parameterizes $f_{\text{esc,abs}}$ as a function of SFR surface density (Σ_{SFR}). For the second model specifically, these authors include $f_{\text{esc,abs}} = 0.09 \pm 0.01$ from **S18** as a constraint in the fit, and predict ~ 10 per cent of sources have $f_{\text{esc,abs}} > 20$ per cent at $z \sim 4$. The Naidu

Table 3. Spectral-fitting parameters from ISM modeling using the ‘holes’ configuration of S18.

Sample ^a	Att	$E(B - V)_{\text{cov}}$	$\log(N_{\text{HI}})$ (cm ⁻²)	f_c	$f_{\text{esc, abs}}$ (S18)	$f_{\text{esc, abs}}$ (this work)
All	SMC	0.161	20.56	0.94	0.09 ± 0.01	0.06 ± 0.01
All, detected ^{b, c}	SMC	0.080	18.59	0.85	0.31 ± 0.03	0.21 ± 0.03
All, not detected	R16	0.160	20.62	0.95	0.05 ± 0.01	0.05 ± 0.01
$W_\lambda(\text{Ly}\alpha) > 0$	SMC	0.056	20.12	0.88	0.14 ± 0.02	0.12 ± 0.02
$W_\lambda(\text{Ly}\alpha) < 0$	R16	0.193	20.98	0.97	<0.03	<0.03
LAEs	SMC	0.052	19.95	0.76	0.29 ± 0.03	0.25 ± 0.03
Non-LAEs	R16	0.170	20.69	0.96	0.04 ± 0.02	0.04 ± 0.01
$L_{UV} > L_{UV}^*$	R16	0.166	20.72	0.96	<0.04	<0.04
$L_{UV} < L_{UV}^*$	SMC	0.064	20.38	0.88	0.13 ± 0.03	0.12 ± 0.03
L_{UV} (Q1)	R16	0.064	20.61	0.93	<0.04	<0.05
L_{UV} (Q2)	R16	0.082	20.79	0.94	<0.04	0.06 ± 0.02
L_{UV} (Q3)	SMC	0.146	20.23	0.92	0.13 ± 0.03	0.08 ± 0.02
L_{UV} (Q4)	SMC	0.153	20.49	0.89	0.16 ± 0.03	0.12 ± 0.02
z (Q1)	SMC	0.076	20.59	0.91	0.08 ± 0.01	0.09 ± 0.01
z (Q4)	R16	0.098	20.36	0.89	0.12 ± 0.02	0.11 ± 0.02
$W_\lambda(\text{Ly}\alpha)$ (Q1)	R16	0.185	21.06	0.97	<0.03	<0.03
$W_\lambda(\text{Ly}\alpha)$ (Q2)	R16	0.202	20.79	0.96	<0.04	0.04 ± 0.02
$W_\lambda(\text{Ly}\alpha)$ (Q3)	SMC	0.056	19.97	0.93	0.07 ± 0.02	0.07 ± 0.02
$W_\lambda(\text{Ly}\alpha)$ (Q4)	SMC	0.049	20.06	0.77	0.27 ± 0.02	0.23 ± 0.02
$(G - R)_0$ (Q1)	SMC	0.021	20.36	0.84	0.15 ± 0.02	0.16 ± 0.02
$(G - R)_0$ (Q2)	R16	0.143	20.56	0.93	0.06 ± 0.02	0.07 ± 0.02
$(G - R)_0$ (Q3)	R16	0.196	20.47	0.95	<0.08	0.05 ± 0.01
$(G - R)_0$ (Q4)	R16	0.274	20.85	0.97	<0.06	<0.03

^aFull composite descriptions can be found in S18.

^bDue to the unique IGM + CGM corrections described in Section 5.1, $f_{\text{esc, abs}}$ is calculated with an additional term for LyC photons traveling through an ISM with order-unity LyC optical depth.

^cAttenuation assumed to be in the lowest 12% of the expected values.

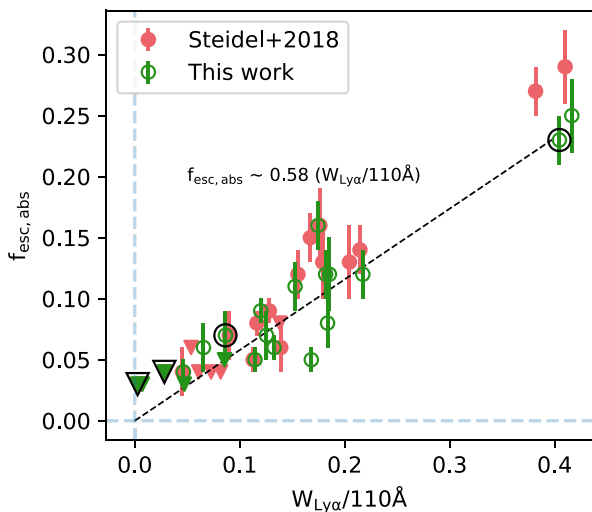


Figure 9. Updated $f_{\text{esc, abs}}$ measurements for the KLCS composites as a function of $W_\lambda(\text{Ly}\alpha)$ alongside values from S18. Each point represents a composite from Table 3. Triangles represent 2σ upper limits on $f_{\text{esc, abs}}$. We fit a linear trend to the four independent quartiles of $W_\lambda(\text{Ly}\alpha)$, highlighted in black, fixing $f_{\text{esc, abs}} = 0$ at $W_\lambda(\text{Ly}\alpha) = 0$.

et al. model would have to be tweaked further to incorporate a lower average $f_{\text{esc, abs}}$ at $z \sim 3$, but the rough percentage of sources with large escape fractions remains consistent with the KLCS detection fraction. This model is also built upon the assumption that the leakage of LyC is correlated with increasing Σ_{SFR} , a determination that can now be tested with the KLCS sample using dust-corrected SFR values and *HST* sizes. In future work, we will focus on the properties of the

LyC leaking galaxies in the uncontaminated KLCS survey, including stellar mass, $E(B - V)$, Σ_{SFR} , and age.

6 SUMMARY

Due to the opacity of the IGM to ionizing photons for $z > 3.5$, direct detections of the LyC in galaxies at lower redshifts are vital for drawing inferences about the ionizing spectra of reionization-era galaxies. With the goal of increasing the number of confirmed individual LyC detections and removing contamination from sample-averaged measurements at $z \sim 3$, we examined LyC detection candidates of the KLCS survey for foreground contamination. By testing each morphological subcomponent for low-redshift signatures with the $V_{606}J_{125}H_{160}$ colour–colour diagram, we removed contaminated objects from the KLCS sample and revisited the measurements of S18 after building uncontaminated composite spectra. The key results are as follows:

(i) We find evidence of foreground contamination in the subcomponents of two LyC detection candidates, Q0933-M23 and Q0933-D16, as well as two non-detections, Q1422-d53 and Q1422-md145. The fraction of contaminated sources within the apparent LyC detections was 2/15, and the subsequent removal of these sources brought the LyC detection fraction for individual objects of the KLCS survey from 15/124 to 13/124.

(ii) We re-measured the sample-averaged ratio of ionizing to non-ionizing rest-UV flux density after performing corrections for IGM and CGM attenuation, finding $\langle f_{900}/f_{1500} \rangle_{\text{out}} = 0.040 \pm 0.006$. This value has been reduced by ~ 30 per cent compared to the original $\langle f_{900}/f_{1500} \rangle_{\text{out}} = 0.057 \pm 0.006$ of S18, indicating the contribution of low-redshift flux density to the KLCS composite spectra. This significant reduction underscores the necessity for high-resolution,

multiband imaging to remove bias in $z \sim 3$ sample-averaged quantities related to the LyC spectrum.

(iii) The strong dependence of $\langle f_{900}/f_{1500} \rangle_{\text{out}}$ on $W_\lambda(\text{Ly}\alpha)$ and L_{UV} within the KLCS sample remains in the contamination-corrected sample. $\langle f_{900}/f_{1500} \rangle_{\text{out}}$ increased from 0.005 ± 0.008 to 0.085 ± 0.014 in composites built from the UV-brightest and dimmest halves of the KLCS sample. We also measured a positive, linear correlation between $\langle f_{900}/f_{1500} \rangle_{\text{out}}$ and $W_\lambda(\text{Ly}\alpha)$ from composite spectra, tying together the escape of LyC and Ly α photons in the ISM of our galaxies.

(iv) We estimated a sample-averaged absolute escape fraction of $f_{\text{esc, abs}} = 0.06 \pm 0.01$ at $z \sim 3$ after performing stellar-population fits and ISM modeling of the rest-UV spectrum. Similar to $\langle f_{900}/f_{1500} \rangle_{\text{out}}$, this uncontaminated value is lower than the S18 $f_{\text{esc, abs}}$ of 0.09 ± 0.01 for the same assumptions concerning the SPS model. We also recovered the positive, linear relationship between $f_{\text{esc, abs}}$ and $W_\lambda(\text{Ly}\alpha)$. This relationship can be interpreted as the H I covering fraction modulating the strengths of both Ly α emission and LyC leakage, supported by relationships between $W_\lambda(\text{Ly}\alpha)$ and f_c that have been found locally (e.g. Gazagnes et al. 2018).

(v) Based on our modified results, we re-estimate the ionizing emissivity of $L_{\text{UV}} > 0.3L_{\text{UV}}^*$ galaxies at $z \sim 3$, determining $\epsilon_{\text{LyC}} \simeq 5.5 \times 10^{24} \text{ erg s}^{-1} \text{ Hz}^{-1} \text{ Mpc}^{-3}$. We perform this calculation using the observed functional dependence of $\langle f_{900}/f_{1500} \rangle_{\text{out}}$ on $W_\lambda(\text{Ly}\alpha)$, the $W_\lambda(\text{Ly}\alpha)$ distribution function, and the FUV luminosity function. Based on this uncontaminated estimate, we conclude that the ionizing background at $z \sim 3$ contains comparable contributions of both galaxies and AGNs.

These results have important implications for models of reionization. Mapping the evolution of the IGM neutral fraction to the change in galaxy populations with redshift requires assumptions of $f_{\text{esc, abs}}$ that must be consistent with direct, sample-averaged results such as those from this work. Moreover, the degree to which $f_{\text{esc, abs}}$ and $\langle f_{900}/f_{1500} \rangle_{\text{out}}$ can be affected by just a few low-redshift interlopers demonstrates the utility of high-resolution follow-up of any individual or statistical detection of $z \sim 3$ LyC. As the sample of confirmed LyC detections widens through deep, spectroscopic and narrow-band imaging surveys, our understanding of the ionizing characteristics of reionization-era galaxies will follow.

ACKNOWLEDGEMENTS

Support for program *HST*-GO-15287.001 was provided by the National Aeronautics and Space Administration (NASA) through a grant from the Space Telescope Science Institute, which is operated by the Associations of Universities for Research in Astronomy, Incorporated, under NASA contract NAS5-26555. CS and YC were supported in part by the Caltech/Jet Propulsion Laboratory President's and Director's program. We wish to extend special thanks to those of Hawaiian ancestry on whose sacred mountain we are privileged to be guests. Without their generous hospitality, most of the observations presented herein would not have been possible.

DATA AVAILABILITY STATEMENT

The *HST* data presented in this article are publicly available from the Mikulski Archive for Space Telescopes. The ground-based data presented here will be shared on reasonable request to the corresponding author.

REFERENCES

- Adelberger K. L., Steidel C. C., Shapley A. E., Hunt M. P., Erb D. K., Reddy N. A., Pettini M., 2004, *ApJ*, 607, 226
- Bertin E., Arnouts S., 1996, *A&AS*, 117, 393
- Bezanson R. et al., 2016, *ApJ*, 822, 30
- Bian F., Fan X., McGreer I., Cai Z., Jiang L., 2017, *ApJ*, 837, L12
- Borthakur S., Heckman T. M., Leitherer C., Overzier R. A., 2014, *Science*, 346, 216
- Bouwens R. J., Illingworth G. D., Oesch P. A., Caruana J., Holwerda B., Smit R., Wilkins S., 2015, *ApJ*, 811, 140
- Bradley L. et al., 2020, *astropy/photutils: 1.1.0*, Zenodo, Available at: <https://doi.org/10.5281/zenodo.4624996>
- Brammer G. B. et al., 2012, *ApJS*, 200, 13
- Calzetti D., Armus L., Bohlin R. C., Kinney A. L., Koornneef J., Storchi-Bergmann T., 2000, *ApJ*, 533, 682
- Chisholm J. et al., 2018, *A&A*, 616, A30
- Cowie L. L., Barger A. J., Trouille L., 2009, *ApJ*, 692, 1476
- De Barros S. et al., 2016, *A&A*, 585, 51
- Du X. et al., 2018, *ApJ*, 860, 75
- Eldridge J. J., Stanway E. R., Xiao L., McClelland L. A., Taylor G., Ng M., Greis S. M., Bray J. C., 2017, *Publ. Astron. Soc. Aust.*, 34, 61
- Fan X., Carilli C. L., Keating B., 2006, *ARA&A*, 44, 415
- Finkelstein S. L. et al., 2019, *ApJ*, 879, 36
- Fletcher T. J., Tang M., Robertson B. E., Nakajima K., Ellis R. S., Stark D. P., Inoue A., 2019, *ApJ*, 878, 87
- Förster Schreiber N. M. et al., 2006, *AJ*, 131, 1891
- Fruchter A. S., Hack W., Dencheva N., Droettboom M., Greenfield P., 2010, Space Telescope Science Institute, Baltimore, MD, p. 382
- Gazagnes S., Chisholm J., Schaerer D., Verhamme A., Rigby J. R., Bayliss M., 2018, *A&A*, 616, 29
- Gordon K. D., Clayton G. C., Misselt K. A., Landolt A. U., Wolff M. J., 2003, *ApJ*, 594, 279
- Hopkins P. F., Richards G. T., Hernquist L., 2007, *ApJ*, 654, 731
- Izotov Y. I., Schaerer D., Thuan T. X., Worseck G., Guseva N. G., Orlitova I., Verhamme A., 2016, *MNRAS*, 461, 3683
- Izotov Y. I., Worseck G., Schaerer D., Guseva N. G., Thuan T. X., Fricke K. J., Verhamme A., Orlová I., 2018, *MNRAS*, 478, 4851
- Izotov Y. I., Worseck G., Schaerer D., Guseva N. G., Chisholm J., Thuan T. X., Fricke K. J., Verhamme A., 2021, *MNRAS*, 503, 1734
- Ji Z. et al., 2020, *ApJ*, 888, 109
- Jones L. H., Barger A. J., Cowie L. L., 2021, *ApJ*, 908, 222
- Kornei K. A., Shapley A. E., Erb D. K., Steidel C. C., Reddy N. A., Pettini M., Bogosavljević M., 2010, *ApJ*, 711, 693
- Kulkarni G., Worseck G., Hennawi J. F., 2019, *MNRAS*, 488, 1035
- Law D. R. et al., 2016, *AJ*, 152, 83
- Mack J., Olszewski H., Pirzkal N., 2021, Space Telescope WFC Instrument Science Report, WFC3/IR Filter-Dependent Sky Flats. Space Telescope Science Institute, Baltimore, Maryland
- Madau P., Dickinson M., 2014, *ARA&A*, 52, 415
- Marchi F. et al., 2017, *A&A*, 601, 73
- Marchi F. et al., 2018, *A&A*, 614, 11
- Momcheva I. G. et al., 2016, *ApJS*, 225, 27
- Mostardi R. E., Shapley A. E., Steidel C. C., Trainor R. F., Reddy N. A., Siana B., 2015, *ApJ*, 810, 107 (M15)
- Naidu R. P., Tacchella S., Mason C. A., Bose S., Oesch P. A., Conroy C., 2020, *ApJ*, 892, 109
- Oke J. B. et al., 1995, *PASP*, 107, 375
- Ouchi M. et al., 2009, *ApJ*, 706, 1136
- Pahl A. J., Shapley A., Faisst A. L., Capak P. L., Du X., Reddy N. A., Laursen P., Topping M. W., 2020, *MNRAS*, 493, 3194
- Parsa S., Dunlop J. S., McLure R. J., 2018, *MNRAS*, 474, 2904
- Parzen E., 1962, *Ann. Math. Stat.*, 33, 1065
- Planck Collaboration, 2016, *A&A*, 594, A13
- Reddy N. A., Steidel C. C., 2009, *ApJ*, 692, 778
- Reddy N. A., Pettini M., Steidel C. C., Shapley A. E., Erb D. K., Law D. R., 2012, *ApJ*, 754, 25

- Reddy N. A. et al., 2015, *ApJ*, 806, 259
- Reddy N. A., Steidel C. C., Pettini M., Bogosavljević M., Shapley A. E., 2016, *ApJ*, 828, 108
- Rivera-Thorsen T. E. et al., 2015, *ApJ*, 805, 14
- Robertson B. E. et al., 2013, *ApJ*, 768, 71
- Robertson B. E., Ellis R. S., Furlanetto S. R., Dunlop J. S., 2015, *ApJ*, 802, L19
- Rosenblatt M., 1956, *Ann. Math. Stat.*, 27, 832
- Scarlata C. et al., 2009, *ApJ*, 704, 98
- Schlegel D. J., Finkbeiner D. P., Davis M., 1998, *ApJ*, 500, 525
- Scott D., 2015, *Multivariate Density Estimation: Theory, Practice, and Visualization*, 2nd edn. Wiley, Hoboken, NJ
- Shapley A. E., Steidel C. C., Pettini M., Adelberger K. L., 2003, *ApJ*, 588, 65
- Shapley A. E., Steidel C. C., Strom A. L., Bogosavljević M., Reddy N. A., Siana B., Mostardi R. E., Rudie G. C., 2016, *ApJ*, 826, L24
- Shen X., Hopkins P. F., Faucher-Giguère C. A., Alexander D. M., Richards G. T., Ross N. P., Hickox R. C., 2020, *MNRAS*, 495, 3252
- Siana B. et al., 2015, *ApJ*, 804, 17
- Skelton R. E. et al., 2014, *ApJS*, 214, 24
- Stanway E. R., Eldridge J. J., 2018, *MNRAS*, 479, 75
- Steidel C. C., Adelberger K. L., Shapley A. E., Pettini M., Dickinson M., Giavalisco M., 2003, *ApJ*, 592, 728
- Steidel C. C., Shapley A. E., Pettini M., Adelberger K. L., Erb D. K., Reddy N. A., Hunt M. P., 2004, *ApJ*, 604, 534
- Steidel C. C., Erb D. K., Shapley A. E., Pettini M., Reddy N., Bogosavljević M., Rudie G. C., Rasic O., 2010, *ApJ*, 717, 289
- Steidel C. C., Strom A. L., Pettini M., Rudie G. C., Reddy N. A., Trainor R. F., 2016, *ApJ*, 826, 159
- Steidel C. C., Bogosavljević M., Shapley A. E., Reddy N. A., Rudie G. C., Pettini M., Trainor R. F., Strom A. L., 2018, *ApJ*, 869, 123 (S18)
- Sunnquist B., 2018, Instrument Science Report WFC3 2018-06, WFC3/IR Blob Monitoring. Space Telescope Science Institute, Baltimore, Maryland
- Van Der Wel A. et al., 2012, *ApJS*, 203, 24
- Vanzella E. et al., 2012, *ApJ*, 751, 70
- Vanzella E. et al., 2016, *ApJ*, 825, 41
- Vanzella E. et al., 2018, *MNRAS*, 476, L15
- Vanzella E. et al., 2020, *MNRAS*, 491, 1093
- Virtanen P. et al., 2020, *Nat. Methods*, 17, 261

APPENDIX A: NON-DETECTIONS

Here we describe the properties of the 24 LyC non-detections targeted by *HST*. In Fig. A1, we show the $V_{606}J_{125}H_{160}$ postage stamps of each non-detection alongside ground-based images, *HST* false-colour images, and segmentation maps in a manner similar to Fig. 3. We report the photometric measurements of each subcomponent displayed in Fig. A1 in Table A1.

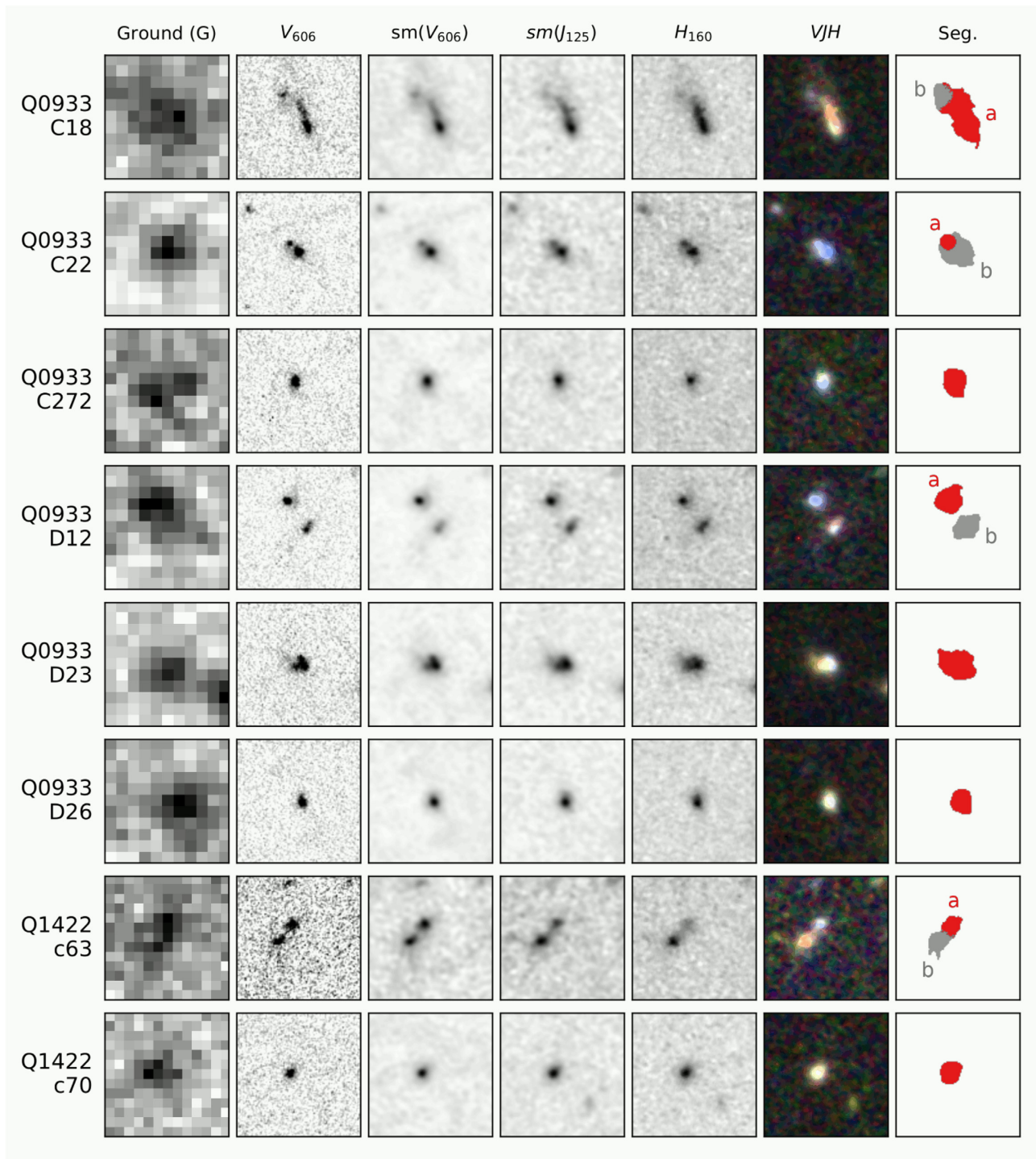


Figure A1. $3 \text{ arcsec} \times 3 \text{ arcsec}$ postage stamps of the 24 LyC non-detections targeted by *HST*. **First column:** Ground-based G (Steidel et al. 2003). **Second column:** V_{606} at the original resolution. **Third and fourth columns:** V_{125} and J_{125} smoothed to the lower-resolution of H_{160} . **Fifth Column:** Original-resolution H_{160} . **Sixth Column:** False-colour postage stamps. The $sm(V_{606})$, $sm(J_{125})$, and H_{160} images are represented by blue, green, and red, respectively. **Seventh Column:** Segmentation map generated by SEXTRACTOR. Separate components extracted by the program are represented by different-coloured regions.

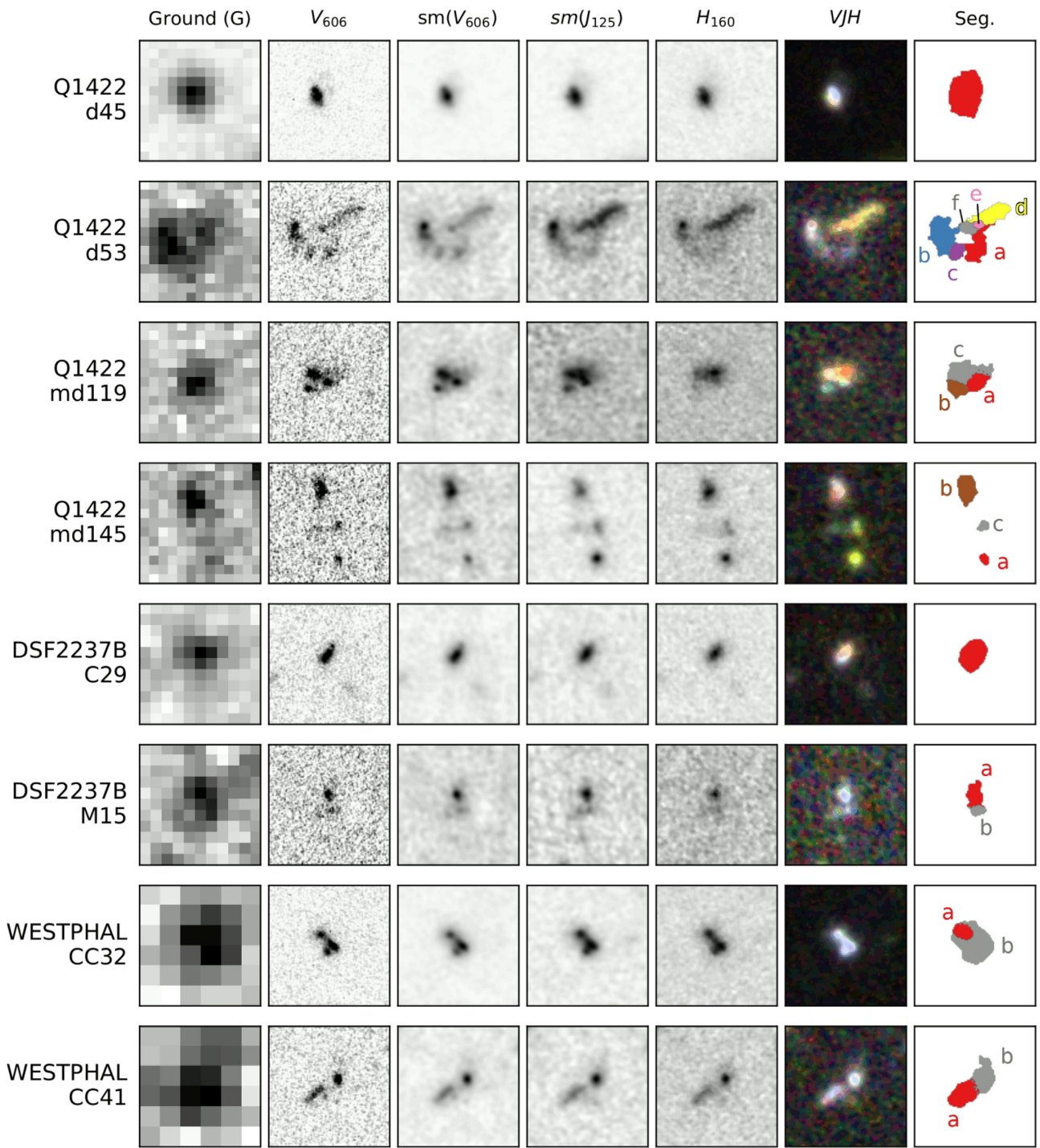


Figure A1 – Continued

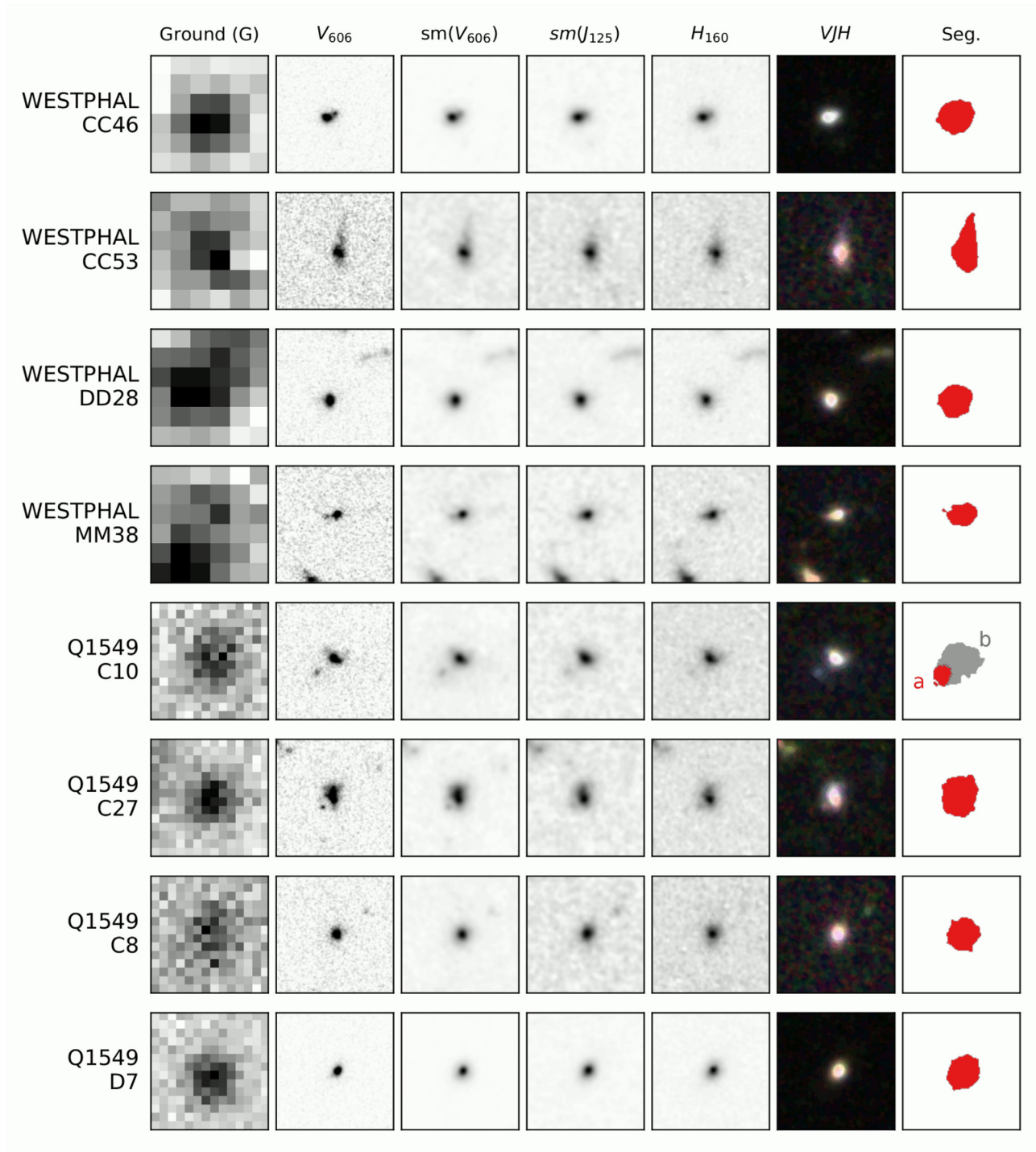
Figure A1 – *Continued*

Table A1. Photometric measurements of the LyC non-detection subcomponents.

ID ^a	R.A.	Dec.	$z_{\text{sys}}^{b,c}$	V_{606}	J_{125}	H_{160}
DSF2237B-C29	22:39:34.50	+ 11:52:41.15	3.100	24.83 ^{+0.04} _{-0.04}	24.88 ^{+0.03} _{-0.03}	24.53 ^{+0.03} _{-0.02}
DSF2237B-M15a	22:39:30.71	+ 11:51:40.93	3.403	26.02 ^{+0.07} _{-0.06}	26.34 ^{+0.07} _{-0.06}	26.44 ^{+0.10} _{-0.09}
DSF2237B-M15b	22:39:30.71	+ 11:51:40.57	3.403	27.45 ^{+0.12} _{-0.11}	27.85 ^{+0.16} _{-0.14}	27.87 ^{+0.20} _{-0.17}
Q0933-C18a	09:33:34.24	+ 28:43:23.39	2.926	24.89 ^{+0.05} _{-0.05}	24.57 ^{+0.04} _{-0.03}	24.06 ^{+0.03} _{-0.03}
Q0933-C18b	09:33:34.28	+ 28:43:23.98	2.926	26.69 ^{+0.09} _{-0.09}	26.66 ^{+0.10} _{-0.09}	26.26 ^{+0.09} _{-0.08}
Q0933-C22a	09:33:32.12	+ 28:43:42.26	3.164	26.53 ^{+0.34} _{-0.26}	26.56 ^{+0.48} _{-0.33}	26.28 ^{+0.51} _{-0.35}
Q0933-C22b	09:33:32.10	+ 28:43:42.08	3.164	25.21 ^{+0.03} _{-0.03}	25.44 ^{+0.04} _{-0.04}	25.31 ^{+0.05} _{-0.05}
Q0933-C272	09:33:27.30	+ 28:44:37.37	3.546	25.42 ^{+0.04} _{-0.04}	25.40 ^{+0.04} _{-0.04}	25.45 ^{+0.06} _{-0.06}
Q0933-D12a	09:33:33.95	+ 28:44:18.83	2.924	25.38 ^{+0.04} _{-0.04}	25.56 ^{+0.05} _{-0.05}	25.36 ^{+0.06} _{-0.06}
Q0933-D12b	09:33:33.92	+ 28:44:18.19	2.924	25.95 ^{+0.06} _{-0.06}	25.95 ^{+0.07} _{-0.06}	25.40 ^{+0.06} _{-0.05}
Q0933-D23	09:33:23.44	+ 28:47:17.11	3.224	24.71 ^{+0.03} _{-0.03}	24.41 ^{+0.02} _{-0.02}	24.12 ^{+0.03} _{-0.03}
Q0933-D26	09:33:25.08	+ 28:48:24.41	3.266	25.34 ^{+0.03} _{-0.03}	25.09 ^{+0.03} _{-0.03}	24.90 ^{+0.04} _{-0.03}
Q1422-c63a	14:24:30.19	+ 22:53:56.52	3.059	26.51 ^{+0.07} _{-0.07}	26.70 ^{+0.09} _{-0.09}	26.40 ^{+0.09} _{-0.08}
Q1422-c63b	14:24:30.22	+ 22:53:56.14	3.059	26.42 ^{+0.08} _{-0.08}	26.18 ^{+0.07} _{-0.06}	25.74 ^{+0.05} _{-0.05}
Q1422-c70	14:24:33.65	+ 22:54:55.27	3.129	25.72 ^{+0.05} _{-0.05}	25.61 ^{+0.04} _{-0.04}	25.32 ^{+0.04} _{-0.04}
Q1422-d45	14:24:32.23	+ 22:54:03.16	3.072	23.77 ^{+0.02} _{-0.02}	23.90 ^{+0.02} _{-0.02}	23.67 ^{+0.02} _{-0.02}
Q1422-d53a	14:24:25.53	+ 22:55:00.28	3.086	26.25 ^{+0.10} _{-0.09}	26.28 ^{+0.09} _{-0.09}	26.08 ^{+0.10} _{-0.09}
Q1422-d53b	14:24:25.59	+ 22:55:00.71	3.086	25.38 ^{+0.06} _{-0.05}	25.45 ^{+0.06} _{-0.05}	25.22 ^{+0.06} _{-0.05}
Q1422-d53c	14:24:25.57	+ 22:55:00.24	3.086	27.13 ^{+0.11} _{-0.10}	27.31 ^{+0.12} _{-0.11}	27.04 ^{+0.13} _{-0.11}
Q1422-d53d	14:24:25.50	+ 22:55:01.22	...	26.12 ^{+0.08} _{-0.07}	25.57 ^{+0.05} _{-0.04}	25.28 ^{+0.04} _{-0.04}
Q1422-d53e	14:24:25.53	+ 22:55:00.92	...	28.48 ^{+0.15} _{-0.13}	27.67 ^{+0.07} _{-0.07}	27.17 ^{+0.06} _{-0.06}
Q1422-d53f	14:24:25.54	+ 22:55:00.83	...	27.56 ^{+0.14} _{-0.13}	27.07 ^{+0.09} _{-0.08}	26.61 ^{+0.07} _{-0.07}
Q1422-md119a	14:24:36.19	+ 22:55:40.33	2.751	26.44 ^{+0.06} _{-0.05}	26.26 ^{+0.07} _{-0.07}	25.92 ^{+0.07} _{-0.06}
Q1422-md119b	14:24:36.22	+ 22:55:40.17	2.751	26.74 ^{+0.06} _{-0.06}	26.70 ^{+0.10} _{-0.09}	26.78 ^{+0.13} _{-0.12}
Q1422-md119c	14:24:36.21	+ 22:55:40.50	2.751	25.73 ^{+0.05} _{-0.05}	25.34 ^{+0.05} _{-0.05}	24.86 ^{+0.04} _{-0.04}
Q1422-md145a	14:24:35.52	+ 22:57:18.53	...	27.78 ^{+0.10} _{-0.09}	26.75 ^{+0.03} _{-0.03}	26.76 ^{+0.04} _{-0.04}
Q1422-md145b	14:24:35.56	+ 22:57:20.26	2.800	25.76 ^{+0.05} _{-0.05}	25.78 ^{+0.04} _{-0.04}	25.34 ^{+0.03} _{-0.03}
Q1422-md145c	14:24:35.53	+ 22:57:19.36	2.800	27.92 ^{+0.12} _{-0.11}	27.45 ^{+0.06} _{-0.06}	27.69 ^{+0.10} _{-0.09}
Q1549-C10a	15:51:48.45	+ 19:09:24.67	3.189	26.84 ^{+0.07} _{-0.07}	27.37 ^{+0.13} _{-0.12}	27.64 ^{+0.23} _{-0.19}
Q1549-C10b	15:51:48.42	+ 19:09:25.01	3.189	24.73 ^{+0.03} _{-0.03}	24.90 ^{+0.03} _{-0.03}	24.72 ^{+0.04} _{-0.04}
Q1549-C27	15:52:07.05	+ 19:12:19.31	2.926	24.42 ^{+0.02} _{-0.02}	24.62 ^{+0.03} _{-0.03}	24.26 ^{+0.03} _{-0.03}
Q1549-C8	15:51:45.39	+ 19:08:49.85	2.937	24.99 ^{+0.03} _{-0.03}	25.15 ^{+0.05} _{-0.05}	24.64 ^{+0.04} _{-0.04}
Q1549-D7	15:51:46.25	+ 19:09:50.10	2.936	24.18 ^{+0.02} _{-0.01}	24.10 ^{+0.01} _{-0.01}	23.73 ^{+0.01} _{-0.01}
Westphal-CC32a	14:18:14.48	+ 52:28:07.26	3.192	26.01 ^{+0.03} _{-0.03}	25.92 ^{+0.03} _{-0.03}	25.71 ^{+0.04} _{-0.03}
Westphal-CC32b	14:18:14.46	+ 52:28:06.99	3.192	24.68 ^{+0.02} _{-0.02}	24.67 ^{+0.02} _{-0.02}	24.49 ^{+0.03} _{-0.03}
Westphal-CC41a	14:18:20.55	+ 52:29:21.14	3.027	26.01 ^{+0.05} _{-0.05}	26.00 ^{+0.06} _{-0.06}	25.62 ^{+0.05} _{-0.05}
Westphal-CC41b	14:18:20.49	+ 52:29:21.48	3.027	26.00 ^{+0.05} _{-0.05}	25.84 ^{+0.05} _{-0.05}	25.57 ^{+0.05} _{-0.05}
Westphal-CC46	14:18:00.20	+ 52:29:53.02	3.261	23.96 ^{+0.01} _{-0.01}	23.76 ^{+0.01} _{-0.01}	23.58 ^{+0.01} _{-0.01}
Westphal-CC53	14:18:22.15	+ 52:30:19.70	2.807	25.22 ^{+0.04} _{-0.04}	25.08 ^{+0.04} _{-0.04}	24.48 ^{+0.03} _{-0.03}
Westphal-DD28	14:18:24.87	+ 52:29:27.32	3.021	24.49 ^{+0.02} _{-0.02}	24.22 ^{+0.02} _{-0.02}	23.83 ^{+0.01} _{-0.01}
Westphal-MM38	14:18:04.07	+ 52:29:54.94	2.925	25.53 ^{+0.03} _{-0.03}	25.16 ^{+0.03} _{-0.03}	24.77 ^{+0.03} _{-0.03}

^aThe field the object is located in, the object name, and a letter corresponding to the subcomponent in Fig. A1. A subcomponent label is omitted in the case of single-component morphology.

^bSystemic redshift from S18.

^cSystemic redshifts are omitted for components predicted as low redshift based on their $V_{606}J_{125}H_{160}$ colours.

This paper has been typeset from a \LaTeX file prepared by the author.